Editors' Suggestion

Charge transport in topological graphene nanoribbons and nanoribbon heterostructures

Mark J. J. Mangnus,[1] Felix R. Fischer,[2,3,4] Michael F. Crommie,[3,4,5] Ingmar Swart,[1] and Peter H. Jacobse[5,*]

[1]*Debye Institute for Nanomaterials Science, Utrecht University, P.O. Box 80000, Utrecht, The Netherlands*

[2]*Department of Chemistry, University of California, Berkeley, California 94720, USA*

[3]*Materials Sciences Division, Lawrence Berkeley National Laboratory, Berkeley, California 94720, USA*

[4]*Kavli Energy NanoSciences Institute at the University of California Berkeley and the Lawrence Berkeley National Laboratory, Berkeley, California 94720, USA*

[5]*Department of Physics, University of California, Berkeley, California 94720, USA*

(Received 12 May 2021; revised 6 March 2022; accepted 7 March 2022; published 23 March 2022)

Although it is generally accepted that structural parameters like width, shape, and edge structure crucially affect the electronic characteristics of graphene nanoribbons (GNRs), the exact relationship between geometry and charge transport remains largely unexplored. In this paper, we present *in situ* through-transport measurements of various topological GNRs and GNR heterostructures by lifting the ribbon with the tip of a scanning tunneling microscope. At the same time, we develop a comprehensive transport model that enables us to understand various features, such as obscuring of localized states in through transport, the effect of topology on transport, as well as negative differential conductance in heterostructures with localized electronic modes. The combined experimental and theoretical efforts described in this paper serve to elucidate general charge transport phenomena in GNRs and GNR heterostructures.

DOI: 10.1103/PhysRevB.105.115424

I. POPULAR SUMMARY

Graphene nanoribbons (GNRs) are narrow, atomically flat strips of carbon atoms in a honeycomb lattice. GNRs exhibit some extraordinary properties, such as high conductivity, highly tunable charge carrier densities, and localized magnetism. These materials hold the potential to supplement or even outperform silicon in integrated circuit architectures, while adding functionality and design opportunities in the form of spintronic devices or qubits for quantum computing.

State-of-the-art GNR manufacturing gives access to a large variety of widths, lengths, and edge structures—properties that govern the electronic, magnetic, and conductance properties. Although the changes in electronic and magnetic properties can readily be measured by experimentalists, the accurate measurement of electron transport remains a challenge. Simply put, it is extremely difficult to attach macroscopic source and drain contacts to microscopic nanoribbons that measure only a millionth of a millimeter across. This challenge has held back our efforts to understand the fundamentals of conductance in GNRs and has prevented us from designing functional nanoribbons that give access to highly desirable electronic and magnetic states.

In this paper, we perform conductance experiments on GNRs in a scanning tunneling microscope (STM) and reveal various phenomena that emerge from charge transport measurements. We develop a transport model that not only captures these effects but is general enough to predict the behavior of a wide range of nanoribbons. The deep level of understanding from our experiments, combined with the predictive quality of the theoretical model, can be used to implement functionalities for the next generation of integrated circuit architectures.

II. INTRODUCTION

GNRs hold promise for use in nanoelectronics due to their exceptional mechanical and electronic properties. Being derived from two-dimensional graphene—a material famed for its unrivaled charge carrier mobility, charge carrier velocity, and spin coherence length [1–4]—exceptional conductance properties also exist in one-dimensional (1D) GNR structures [5]. In contrast with zero-gap semimetallic graphene, GNRs typically feature a finite bandgap, opening a path to functionalized structures that display switching, rectification, spintronic, or field-effect transistor (FET) behavior [5–20].

GNRs are not only interesting regarding electronics but may also harbor magnetic functionality. It has been realized that the zigzag edges of nanographene give rise to sublattice-polarized states, which are prone to spin splitting by the Stoner mechanism. Magnetic and spintronic properties can be implemented in GNR architectures by rational engineering of the edge structure [21–30]. Recent experiments have revealed magnetic phenomena in nanographenes and GNRs through fingerprints like Kondo resonances and singlet-triplet excitations in inelastic tunneling spectroscopy measurements [31–40]. An idea that has recently gained traction in the field relies on zero modes—states near the Fermi energy—that can be tuned at will in GNR architectures through the concepts of sublattice imbalance engineering and topology [41–46]. Depending on the exact GNR design, these

*jacobse@berkeley.edu

states may be occupied by single-electron spins that are magnetically coupled through the π-backbone of the ribbon. This creates an opportunity for controlling magnetic properties that might eventually lead to the development of GNR-based device architectures meeting the stringent requirements for spintronics-based quantum information processing [47].

The synergy of electronic and magnetic functionality in GNRs is not only appealing for the design of the next generation of faster, smaller, and more energy-efficient carbon-based nanoelectronics but even holds the key to accessing complex computing architectures such as quantum computing. Other interesting effects that have recently been unveiled in GNRs are the modulation of current by edge defects [48], molecules, or fused groups [49–52]. Mechanosensors [53,54] and nanomeshes have also been conceived [55–58]. Robust metallicity [46] and negative differential resistance (NDR), a phenomenon required for creating resonant diodes and oscillators [8,59–67], can be engineered. Tunable electroluminescence and photoconductance in GNRs close the gap between GNR electronics and photonics [68–71]. In every case, the high tunability of the intrinsic properties of GNRs afforded by the rational design and engineering of the atomic structure sets nanoribbons apart and is a stark contrast to the less malleable properties associated with traditional, three-dimensional inorganic semiconductors [72–76].

Despite the advances in GNR fabrication over the past decade, it remains a challenge to measure a key characteristic of GNRs: their transconductance (electron transport through the GNR backbone). Conductance in an STM setup is typically measured perpendicular to the GNR rather than through its backbone and fails to identify transport effects related to localization and consequent mobility modulation. Three general strategies are currently being pursued to overcome the main difficulty of accessing GNR transconductance, which may intuitively be thought of as the challenge of attaching nanometer-scale probes to a single GNR. The first strategy relies on the transfer of GNRs from their metallic growth substrate to a prefabricated device architecture [9,77–80]. Unfortunately, measurements on GNRs transferred to devices lack information on the exact identity and structure of the nanoribbon (or bundle or network of nanoribbons) being probed and often return data that reveal more about the relative Fermi level alignment and Schottky barrier effects than the inherent, quantum-mechanical transport in a single GNR. A second technique addresses the charge carrier mobility and mean-free path through terahertz photoconductivity [81–83]. This technique probes intrinsic conductance characteristics of the nanoribbon yet has the downside that it also probes excitonic behavior and does not correspond to a realistic nanoelectronics device geometry (where the electronic properties of the GNR are accessed through direct injection of carriers from electrical leads). A third technique is the *in situ* lifting of individual GNRs inside the STM by controlled attachment of the probe to one end of the ribbon and forcing the tip-substrate current to pass through the GNR backbone [30,37,65,69,84–87]. A drawback here is the inability to gate the system. These techniques remain challenging to this day, with the result that GNR transport and the more exotic (spin) transport effects of specific rational GNR designs remain largely unexplored. This represents a scientific dilemma, as promising theoretical transport models remain largely unverified by experiments. It is therefore crucial to expand our understanding of GNR conductance to advance the design of GNRs with interesting electronic and magnetic functionality.

Herein, we present a combined experimental and theoretical approach that paves the way to a deeper understanding of transport through GNRs. We present data on transport through different types of ribbons as measured by *in situ* STM lifting. The nanoribbons that we address experimentally are 5-atom-wide armchair GNRs (5-AGNRs), 7-AGNRs, and heterostructures of these. Transport characteristics are simulated via calculations using the nonequilibrium Green's function technique (NEGF) applied to a mean-field Hubbard (MFH) tight-binding model. This model is implemented in MATHEMATICA using the MATHEMATB package [88]. We present the models and experiments in the context of recent discoveries such as 1D GNR topology, the emergence of NDR in GNR heterostructures, and the discovery of magnetic fingerprints in GNR transport. Sections III A–III C of this paper detail case studies where a zero-bias treatment suffices to describe the transport phenomena, while electrostatics—necessary to understand effects at higher bias—is the focus of the second part (Sec. III D). The uniqueness of our model is that it has an atomistic basis instead of being purely effective and captures all the relevant physics but does not use any of the black box approaches of established first-principles calculations, instead laying bare the entire machinery of the calculation in the process. The aim of this paper is twofold. First, our results and accompanying model serve to elucidate transport in specific cases. Secondly, the extension of prototypical results to various types of GNRs—accompanied by a discussion of various electronic and magnetic effects in these structures—serves to advance the understanding of GNR transport in general.

III. RESULTS

A. Transport in a 7/14/7-AGNR quantum dot: Local density of states vs transconductance

1. Measurement of the charge transport in a 7/14/7-AGNR quantum dot

We start by analyzing the transport in a bottom-up synthesized 7/14/7-AGNR quantum dot: a heterostructure composed of a 14-atom-wide AGNR segment sandwiched in between two 7-atom-wide leads. While 7-AGNRs are wide-gap semiconductors of the $N = 3p + 1$ family, where p is a positive integer ($p \in \mathbb{N}$), 14-AGNRs, like 5-AGNRs, belong to the low-gap $N = 3p + 2$ family of AGNRs [6,7]. The $3p + 2$ rule can intuitively be understood as the result of projecting the graphene dispersion along lines in the Brillouin zone with a discrete transverse wave number, in which case the Dirac point (and hence zero bandgap) is included only if the number of atomic rows is $3p + 2$. It has indeed been established that 7/14/7-AGNRs behave as GNR quantum dots, with several low-energy states localized on the 14-AGNR segment that are within the bandgap of the 7-AGNR leads [89].

We synthesized 7/14/7-AGNRs following the procedure of Wang *et al.* [89] (procedure given in Sec. 1 of the Supplemental Material [90]; see also Refs. [22,65,86,89,91–94] therein).

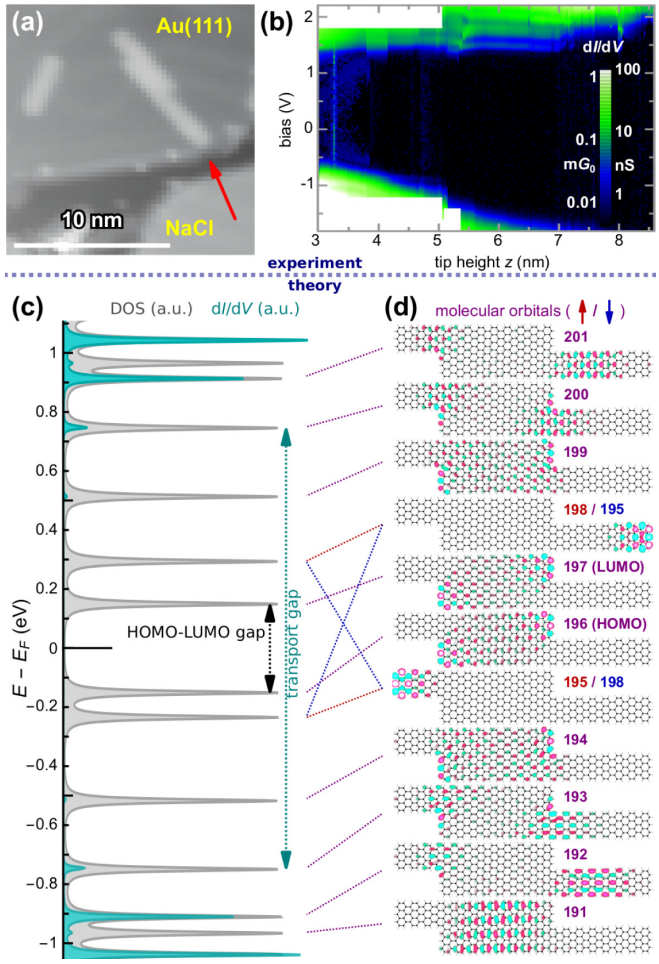

FIG. 1. Relationship between eigenstate localization, density of states (DOS), and transport probed in a 7/14/7-armchair graphene nanoribbon (AGNR). (a) Scanning tunneling microscope (STM) topographic scan ($V = -1.2$ V, $I = 20$ pA) of a 7/14/7-AGNR on Au(111), next to a NaCl island. The arrow denotes where the STM tip was attached for conductance measurements. (b) Map of the differential conductance $dI/dV(V, z)$ for the ribbon in (a), lifted on the NaCl island. (c) Calculated zero-bias transport from tip to surface (teal), employing an extra Lorentzian broadening of 2 meV, and DOS (gray). The highest occupied molecular orbital (HOMO)–lowest unoccupied molecular orbital (LUMO) gap and transport gap are indicated. (d) Calculated molecular orbitals of frontier states 191 to 201. Orbitals 195 and 198 are reversed for the spin-down eigenstates (blue labels) compared with the spin-up eigenstates (red labels), as indicated; all other states are the same for the two spin channels (purple labels).

Figure 1(a) shows an STM image of a 7/14/7-AGNR on Au(111), next to an island of NaCl which was codeposited as a means of providing an insulating intercalant that preserves the intrinsic electronic properties of the GNR which may otherwise be affected by coupling to the metallic substrate. We first contacted the STM tip to the end of the nanoribbon [red arrow in Fig. 1(a)] and subsequently manipulated the ribbon horizontally onto the NaCl island before performing measurements of the differential conductance dI/dV (the methodology is given in more detail in Sec. 1 of the Supplemental Material [90]) [86]. The conductance map, shown in Fig. 1(b), reveals onsets of ballistic transport at $V < -1$ V and $V > 2$ V for low tip heights, identical to the result for pristine 7-AGNRs on NaCl [86]. The tip height was increased from 3 to ∼9 nm, which is longer than the length of the 7-AGNR segment of this heterostructure (4 nm). In this geometry, the current is forced to traverse not only the 7-AGNR segment but also the 14-AGNR segment. A slight widening of the transport gap is evident, in agreement with previous work [86], yet the transport profile remains gapped with no evidence of lower energy states contributing to the current.

2. *Simulation of the charge transport in a 7/14/7-AGNR quantum dot*

(a) Model. Figure 1(c) shows the total density of states (DOS) in gray for the 7/14/7-AGNR as calculated by a zero-bias transport model (Sec. 1 of the Supplemental Material [90]), based on the NEGF approach. The electronic structure was obtained by applying the following atomistic MFH Hamiltonian:

$$\hat{H} = \sum_{i,\sigma}^{\text{sites}} \varepsilon_0 c_{i,\sigma}^{\dagger} c_{i,\sigma} + \sum_{\langle i,j\rangle,\sigma}^{\text{pairs}} t_{ij}(c_{i,\sigma}^{\dagger} c_{j,\sigma} + c_{i,\sigma}^{\dagger} c_{j,\sigma}) + \sum_{i}^{\text{sites}} U(n_{i\uparrow}\langle n_{i\downarrow}\rangle + \langle n_{i\uparrow}\rangle n_{i\downarrow} - \langle n_{i\uparrow}\rangle\langle n_{i\downarrow}\rangle), \quad (1)$$

to a minimal basis of carbon p_z orbitals. To simulate the coupling of the GNR to the surface, all diagonal elements of the surface self-energy matrix Σ are set equal to $i(\gamma/2) = 10i$ meV. The energy-independent nature of Σ is known as the wide-band limit, which is valid when the DOS of the metal is relatively flat within the energetic region of interest and the coupling of GNR states to the metal is relatively energy independent [95]. As shown in Sec. 2 of the Supplemental Material [90], the DOS for each spin channel consists simply of Lorentzians of full width at half maximum of 10 meV, centered around the eigenenergies ε_{orb}:

$$\text{DOS}_{\sigma}(E) = \frac{1}{\pi} \sum_{\text{orb}} \frac{\left(\frac{\gamma}{2}\right)}{(E - \text{Re}[\varepsilon_{\text{orb},\sigma}])^2 + \left(\frac{\gamma}{2}\right)^2}. \quad (2)$$

Like most GNRs, the π-electron energy spectrum of the 7/14/7-AGNR exhibits electron-hole symmetry which is a consequence of the bipartite nature of the honeycomb lattice (see Sec. 3 of the Supplemental Material [90]; see also Refs. [26,27,96,97] therein).

(b) Results. Figure 1(c) also shows the simulated transport (dI/dV) (teal curve). In this calculation, only the 175 leftmost atoms were assumed to be in contact with the surface (corresponding to approximately half of the ribbon), and the rightmost atom was coupled to the tip. An extra Lorentzian broadening of $\gamma = 2$ meV was applied to smoothen the extremely narrow peaks obtained for the transmission in a more continuous function, helping to visualize the spectrum. There may be other physical mechanisms at work that cause more significant spectral broadening. Figure 1(d) shows the molecular orbitals. In agreement with the experiment of Wang *et al.* [90], the model reproduces the low-energy states on the 14-AGNR segment. These are orbitals 193 to 200 in Fig. 1(d), where orbital 196 is the highest occupied molecular

orbital (HOMO) and orbital 197 is the lowest unoccupied molecular orbital (LUMO) for a charge-neutral system (resulting in a 0.3 eV HOMO-LUMO gap). The 14-AGNR states are interspersed by the two end states on the two 7-AGNR ends (orbitals 195 and 198, which are reversed for the two spin channels, as indicated by the labels) [26,98–100]. The orbitals localized on the ends and on the 14-AGNR segment (orbitals 193 to 200) span the energy range between $E - E_F = -0.8\,\text{eV}$ and $E - E_F = 0.8\,\text{V}$, with no eigenstates delocalized over the 7-AGNR leads in this window.

Although present in the DOS, the states localized on the 14-atom-wide center segment are largely suppressed in the transport, as can be seen both in the experiment as well as in the calculated transport [teal spectrum in Fig. 1(c)]. The transport gap spans $\sim$1.5 eV in the calculation, in stark contrast with the small theoretical HOMO-LUMO gap and in good agreement with the theoretical transport gap of pure 7-AGNR (without taking addition energy and quasiparticle renormalizations into account). Thus, both the theory and experiment reveal an occlusion of states from the transport profile that are not well connected to the tip. Although easy to understand, the vastly different dI/dV probed in standard scanning tunneling spectroscopy (STS) and in through-transport measurements is a striking result that highlights the difference between local DOS (LDOS) and transport through the length of a nanoribbon. Whereas STS can be understood to represent the LDOS, as per the interpretation of Tersoff and Hamann [101], transport can effectively be understood to be a weighted form of the LDOS, where the weights are the transmission probabilities for each channel or conductance orbital, which represent the connectedness of the orbitals between tip and surface. Equivalently, these are electron mobilities: in band theory, flat bands represent heavy carriers that are more localized, and in a finite-sized system, the corresponding orbitals are not well connected to the tip and surface simultaneously because of this tendency to be localized [102]. Notice that, in this regard, the MFH term in the Hamiltonian plays an important role, as it helps to properly describe the localization of eigenstates. If the MFH term would be omitted, no spin splitting of the end states would be predicted, and they would instead appear as symmetric and antisymmetric combinations of the left- and right-localized end state orbitals, thus falsely suggesting eigenstates that connect to both tip and surface simultaneously and wrongfully returning a zero-bias conductance peak.

(c) Implications for general transport in GNRs. Note that, in general, if an electronic component, molecule, or other functional structure is contacted with GNR leads, its electronic functionality cannot be accessed if the corresponding energy levels are within the transport gap of the leads. A refinement to this rule should be given in the case where the leads are short enough to carry significant off-resonant transport. The exponentially decaying tail of an electron may still be long enough even when the electron does not hit a resonance of the lead but is close to it in energy. This occurs more readily in narrow-gap nanoribbons, such as the 3,1-chiral GNR. An example of this scenario comes from Li *et al.* [103], who managed to access the spin of a magnetic molecule contacted by 3,1-chiral GNRs through off-resonant transport. In this case, the short GNR lead length and low bandgap provide the necessary ingredients to probe the molecule through tunneling. Nevertheless, since off-resonant transport will decay with increased path length through a GNR, off-resonant transport is not useful for systems with arbitrary long leads [84,86].

B. Transport in 5-AGNRs: Open vs closed shell

1. *Topological nature of 5-AGNRs and effect on charge transport*

(a) Open-shell character induced by nontrivial topology. In this section, we switch to a different GNR: the 5-AGNR. 5-AGNRs belong to the $N = 3p + 2$ family of narrow-gap AGNRs. Their relatively small bandgap makes them interesting candidates for FETs, and as a result, they have seen some recent research interest regarding their transport properties. Also, 5-AGNRs are understood to have a finite bandgap that can be attributed to the dimerization of carbon atoms along the edges. This interaction lowers (raises) the energy of frontier crystal orbitals that exhibit cusps (nodes) between carbon dimers, leading to a gap in the projected dispersion around the Dirac point [7]. The relatively narrow gap causes the frontier bands to remain dispersive, meaning that charge carriers injected into the valence or conduction bands are lighter than those injected into wider-gap nanoribbons. Interestingly, 5-AGNRs also have some topological properties. In general, the chemically distinct nature of the A and B sublattices at the zigzag edge (one of them protruding and hydrogen capped, the other one having bulklike characteristics) can trigger the formation of emergent sublattice-polarized states, known as zero modes since they straddle the Fermi energy [41–46]. Given the standard perylene/naphthalene-type termination, 5-AGNRs have a topological invariant of $\mathbb{Z}_2 = 1$, corresponding to a 180 ° Zak phase [41,44]. Since vacuum is topologically trivial, 5-AGNRs are expected to exist as an open-shell, biradical structure, with a pair of low-energy zigzag end-localized states at charge neutrality, like 7-AGNRs [41]. The open-shell nature of long 5-AGNRs was recently verified by Lawrence *et al.* [37], who not only characterized the adsorbed nanoribbons but also performed lifting experiments. The large work function of the Au(111) surface acts to extract electrons and to leave the nanoribbon positively charged. The act of lifting the nanoribbon from the surface with the STM tip then replenishes the initially vacant end state at sufficient tip height from the gold surface. As shown in Fig. 2(a), evidence of this comes from the observation of shifting of the end state level through the Fermi level from positive to negative energy with increasing tip height, and the emergence of a Kondo resonance, which is a magnetic fingerprint of the interaction of an unpaired electron on the GNR with itinerant electrons in the tip and indicates that the corresponding state becomes singly occupied [104,105].

(b) Effect of open- or closed-shell configuration on transport. Figure 2(b) shows the calculated frontier orbitals for a 5_{14}-AGNR and a 5_8-AGNR (here, the subscript denotes the number of repeating naphthalene units). The longer 5_{14}-AGNR reveals an open-shell ground state in its frontier orbitals, with a pair of degenerate singly occupied molecular orbitals (SOMOs) and singly unoccupied molecular orbitals (SUMOs) in which the spin-up and spin-down electrons reside on opposite ends. By contrast, the shorter 5_n-AGNR has a closed-shell character with a doubly occupied, delocalized HOMO and vacant LUMO level

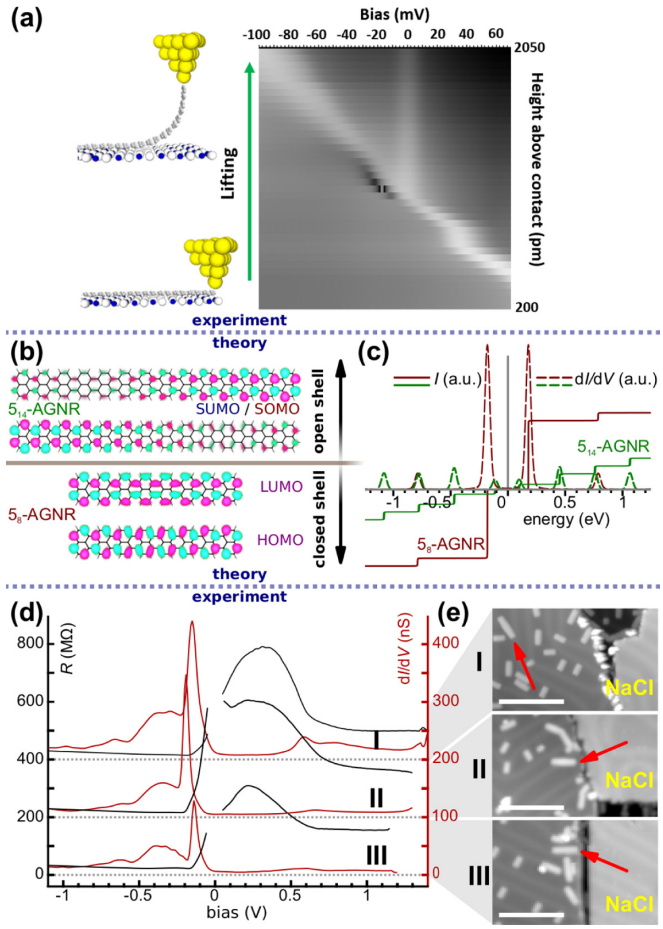

FIG. 2. Transport in open- and closed-shell 5-armchair graphene nanoribbons (AGNRs). (a) Transport in a long 5-AGNR as a function of tip height and bias voltage. Reproduced with permission from Lawrence *et al.* [37]. (b) Calculated frontier orbitals of the 5_{14}-AGNR and 5_8-AGNR, respectively, revealing an open-shell ground state in the former and closed-shell ground state in the latter. (c) Calculated $I(V)$ (solid) and dI/dV (dashed) transport for the 5_8-AGNR (red) and 5_{14}-AGNR (green). The dI/dV was Gaussian-broadened by 20 meV. (d) Transport dI/dV and resistance R measured in three different 5-AGNRs, labeled I, II, and III. Spectra are offset by 100 nS (200 MΩ). (e) Scanning tunneling microscope (STM) topographic scans ($V = -1.2$ V, $I = 20$ pA) of the three 5-AGNRs whose transport is shown in (c). The arrows indicate the position where the tip was contacted to the GNR end. All scale bars are 10 nm.

straddling the gap. Figure 2(c) shows the calculated transport characteristics of closed-shell 5_8-AGNR and open-shell 5_{14}-AGNR. In both calculations, a tip was connected to a single atom on the right with strength $\sigma_{\text{tip}} = i(\gamma/2)_{\text{tip}} = 67i$ meV, and the left half of the ribbon was connected to the surface through the NaCl with strength $\sigma_{\text{NaCl}} = i(\gamma/2)_{\text{NaCl}} = 10i$ meV. Interestingly, the transport is dominated by the frontier states for the shorter 5_8-AGNR, with the corresponding transport resonances significantly larger than all other resonances, while for the longer 5_{14}-AGNR, the situation is reversed. This stems from an increased tip-orbital coupling for the frontier-state wave functions, which feature a higher density toward the ends, resulting in a more intense broadening of the frontier-state transport resonance. Even though the transmission T maxes out at 1 for both frontier states and states at other energies (indicating a fully open channel permitting a conductance quantum), it is the enhanced peak width that ultimately gives a higher current after integration of the conductance as per the Landauer-Büttiker formula:

$$I_\sigma(V) = \frac{G_0}{e}\int_{-\infty}^{\infty} T_\sigma(E)[f(E-\mu_0) - f(E-\mu_V)]dE. \quad (3)$$

where μ_0 and μ_V are the chemical potentials of the surface (assumed to be at zero bias) and tip (assumed to be at a bias V). For the 5_{14}-AGNR, the frontier orbitals are no longer delocalized but spin split, and neither end state has simultaneous high density on the atoms in contact with the surface and the tip: therefore, frontier-state transport is suppressed.

We would like to emphasize that the nature of the contacts is asymmetric: presumably covalent for the tip-GNR junction and a weak van der Waals-type contact for the GNR-substrate junction. In practice, however, this has only little effect on the GNR electronic structure and transport, as experimentally suggested by the retention of fingerprints of the arguably delicate end states of both the 5-AGNR [37] and the 7-AGNR [69] in lifting experiments. Moreover, in the case of the 7-AGNR, density functional theory calculations have suggested that, even though each end state may lose its SOMO-SUMO gap, they are still extant and spatially localized on either end even after a covalent carbon-gold covalent bond is formed between the tip and ribbon [69].

2. *Charge transport experiments on 5-AGNRs*

(a) Observation of enhanced frontier-state conductance. Here, 5-AGNRs were synthesized and subjected to transport measurement in accordance with Refs. [37,65,86,106]. The GNRs selected for transport measurements are shown in Fig. 2(e) and are ∼3 to 3.5 nm in length, corresponding to 7 or 8 repeating units. Figure 2(d) shows the differential conductance (dI/dV) and resistance (R) measured for the three ribbons shown in Fig. 2(e) on NaCl. The transport was measured after lifting the GNRs on NaCl to a height of 2 nm, which is in the Kondo regime of Lawrence *et al.* [37]. A clear and reproducible transport gap of 0.75 V is found between the onset of hole tunneling at $V = -0.15$ V [called the positive ion resonance (PIR)] and electron tunneling $V = 0.6$ V [negative ion resonance (NIR)]. The PIR is much stronger than all other features in the spectra, in agreement with the prediction for the shorter 5-AGNR in Fig. 2(b), although we are not certain about the mechanism that dampens the expected strong resonance for the NIR. Note that additional detailed features of the spectra [Fig. 2(e)]—which may be interpreted as off-frontier transport resonances combined with vibrational fine structure—are completely reproducible. This is particularly striking when considering that the STM tip was subjected to restructuring through repeated indentation into the surface in between experiments.

(b) Relation to open-shell and device transport measurements. The transport we measured is strikingly different from that obtained by Lawrence *et al.* [37]: The absence of a Kondo resonance indicates that there is no singly occupied orbital in contact with either tip or gold surface and therefore suggests that the 5-AGNRs measured are indeed closed shell.

Moreover, we find enhanced transport for the PIR compared with higher-bias resonances, which agrees with the transport simulations that suggested a dominating contribution from the frontier states in the case of shorter nanoribbons (even though the relative dampening of the transport at positive bias is not yet well understood). An apparently similar phenomenon was also recently found in charge transport in 5-AGNR/graphene nanogap devices by El Abbassi *et al.* [80] In their experiment, the transport was measured in 5-AGNRs spanning an electroburnt graphene gap, in the Coulomb blockade regime, where the dominating resistance is the electrode-GNR contact resistance and the subsequent variations in conductance are proportional to the inherent, weakly coupled electronic structure of the 5-AGNR. The graphene electrodes gave a good match to the work function of the GNR and counteracted Schottky barrier effects that may be present in metal-GNR junctions. In apparent agreement with our results, they reported enhanced transport in shorter 5-AGNRs and concluded that this similarly resulted from the contribution of the end states. Nevertheless, the non-UHV conditions of their experiment mean that atmospheric oxidation or other contamination cannot be ruled out, and a one-to-one comparison between our experiment and theirs may be misleading. In our experiment, we know for sure that the GNRs we measure are pristine, so our measured transport characteristics can now be correlated directly to the intrinsic electronic structure of the GNR.

C. Transport in topological nanoribbons: Spin splitting vs transmission

1. General dependency of frontier-state transport on ground state

Localized states give rise to opaque transport resonances in transmission spectra: this was proven for the in-gap states of the 7/14/7-AGNR quantum dot as well as for the topological end states for long 5-AGNRs. This suggests that the zero-bias transmission is intricately correlated with the open- or closed-shell ground state of topological GNRs. In this section, we generalize the interplay between topological nanoribbons and transport by studying transport in 5_n-AGNRs in comparison with 7_n-AGNRs, 9_n-AGNRs, and 11_n-AGNRs. These GNRs represent the three families of armchair-type nanoribbons: the intermediate-gap $N = 3p$, the wide-gap $N = 3p + 1$, and narrow-gap $N = 3p + 2$. The 11-AGNR is included for the sake of it having a different topology than the narrower 5-AGNR—with $\mathbb{Z}_2 = 0$ for the same termination—even though they belong to the same $N = 3p + 2$ family [41].

Figure 3(a) shows the results of zero-bias transmission calculations on N_n-AGNRs of length $n = 1$–24, with the different rows corresponding to widths $N = 5, 7, 9$, and 11. The first column shows the frontier orbitals for the N_2-AGNRs and the N_6-AGNRs, respectively. Here, it is evident that the 5-AGNR is closed shell for both lengths [consistent with Fig. 2(b)], but the 7-AGNR is open shell for the longer ribbon. In the case of the 9-AGNR and 11-AGNR, there is already significant splitting occurring even for the N_2-AGNRs. Interestingly, in the case of the 11_6-AGNR, the frontier states have a delocalized character. Further study reveals that the off-frontier states are end localized (not shown).

The second column of Fig. 3(a) shows the calculated transmission for either spin channel σ for the N_2-AGNRs (red) in comparison with the N_6-AGNRs. In the transport calculations, we used couplings of $i(\gamma/2)_{\text{tip}} = 33i$ meV to the 2 ($N = 5$), 3 ($N = 7$), 4 ($N = 9$), or 5 ($N = 11$) protruding zigzag atoms on both ends of the GNR. The impact of the localized/delocalized character on the transmission is evident. Whereas fully delocalized orbitals have an associated peak in the transmission $T_\sigma(E)$ of exactly unity—corresponding to an open channel that permits the transport of a conductance quantum—the localized channels exhibit lower conductance peak values. The frontier states of the 5_2-AGNR and 5_6-AGNR are fully open, but the frontier states of the 7_2-AGNR have an associated conductance that falls from 1 to 0.01 as n is increased from 2 to 6. The frontier-state conductance falls off even more quickly for the 9-AGNR and cannot even be distinguished at all for the 11-AGNR. Even though the bandgaps of the 9-AGNR and 11-AGNR are smaller than that of the 7-AGNR, the increased lateral delocalization of the end states over the zigzag edge of the terminus of the ribbon acts to decrease the effective coupling t_{eff} between end states.

The transmission is shown for all N_n-AGNRs as a function of energy and length n in the third column of Fig. 3(a). For low n, the frontier-state transmission peaks shift toward the Fermi energy, followed by their gradual disappearance. This then results in a transport gap spanned not by the frontier orbitals but by the off-frontier states. The 7-AGNR transport gap established in Sec. III A, between $V = -0.8$ and 0.8 V shows up, as well as a 0.6 V transport gap for the 5-AGNR, a 0.85 V transport gap for the 9-AGNR, and a 0.5 V transport gap for the 11-AGNR. Note that, unlike the relative conductance of the frontier states to bulk states in short 5-AGNRs as explored in Sec. III B, the impeded transport through the frontier states is not a manifestation of relative peak widths of resonances that max out at the conductance quantum but rather of frontier peaks that have a suppressed conductance maximum. This happens when the orbital localization gives rise to an asymmetric coupling to the electrodes, such that the overlap between the spectral density $\mathbf{A}$ and coupling to the other electrode $\mathbf{\Gamma}$ is suppressed (see Sec. 4 of the Supplemental Material [90]):

$$\begin{aligned} T(E) &= \text{tr}[\mathbf{\Gamma}_0 \mathbf{G}^-(E) \mathbf{\Gamma}_V \mathbf{G}^+(E)] \\ &= \text{tr}[\mathbf{\Gamma}_0 \mathbf{A}_V] = \text{tr}[\mathbf{\Gamma}_V \mathbf{A}_0]. \end{aligned} \tag{4}$$

2. Understanding the magnetic phase transition

(a) The effective Hubbard model. Above a certain length n, the topological frontier states of an N_n-AGNR split up as they undergo a phase change from a closed-shell (diamagnetic) to an open-shell (antiferromagnetic) ground state, and consequently, their transmission falls <1 due to the localized nature of these orbitals. Figure 3(c) summarizes these results, as it shows the transmission through the frontier orbital as a function of number of repeating units n. Here, the initial unimpeded transmission, followed by a sudden decaying transmission as the GNR goes into an open-shell ground state, is shown for the different widths N of the N-AGNRs. It should be noted that the transition to an open-shell ground state is correlated with the emergence of a Kondo resonance at zero bias, but such features are not captured in the Hubbard model and would require a treatment at the level of the Anderson

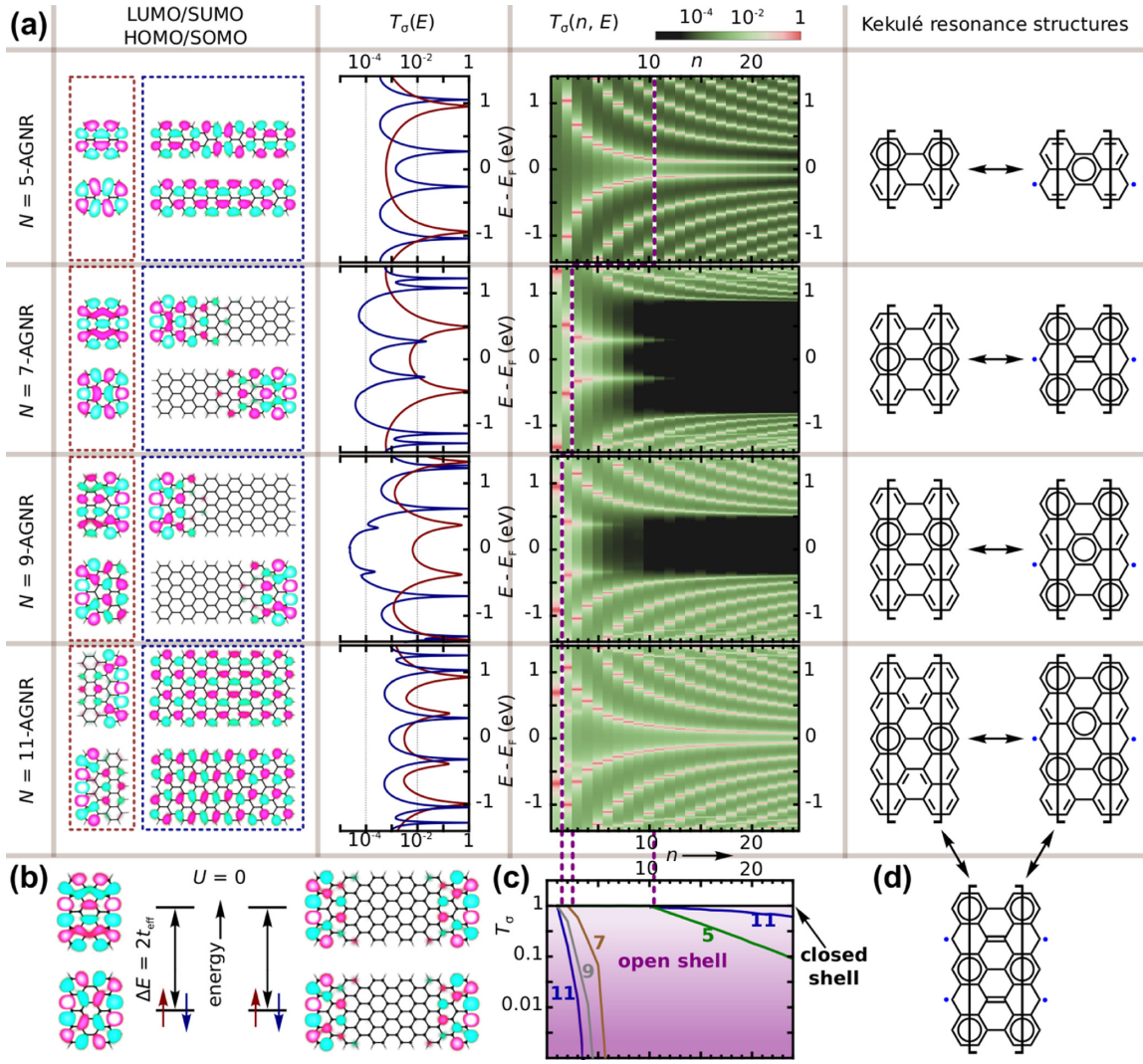

FIG. 3. Relationship between graphene nanoribbon (GNR) topology, ground state, end states, and zero-bias transmission. (a) Table showing calculated frontier states for the N_2-armchair GNR (AGNR) and N_6-AGNR (first column), calculated zero-bias transmission for the N_2-AGNR (red) and N_6-AGNR (blue) as a function of energy (second column), zero-bias transmission for N_n-AGNRs as a function of length n (third column), and Kekulé resonance structures corresponding to the closed- and open-shell configurations of N-AGNRs. The rows correspond to the $N = 5$-AGNR, 7-AGNR, 9-AGNR, and 11-AGNR, respectively. (b) Tight-binding calculation employing $U = 0$ for the 9_2-AGNR and 9_6-AGNR. The frontier states are shown, with a schematic energy diagram. (c) Calculated transmission of the frontier states of 5_n-, 7_n-, 9_n-, and 11_n-AGNR as a function of length n. (d) Doubly open-shell Kekulé resonance structure for the 11-AGNR.

impurity model [107,108]. In general, the closed- to open-shell threshold is determined by a competition between the effective hybridization energy t_{eff} and effective Coulomb interaction U_{eff} [22]: If t_{eff} is small relative to U_{eff}, GNRs will prefer to exist in an open-shell ground state. If this is the case, then the exchange interaction between the unpaired spins in turn becomes $J = 4t_{\text{eff}}^2/U_{\text{eff}}$ [109].

The parameters U_{eff} and t_{eff} can be extracted from the calculation, by artificially switching off the Hubbard U. This is shown in Fig. 3(b), where the calculation with $U = 0$ is performed on the 9_2-AGNR and 9_6-AGNR. Without Coulomb interaction, the end states hybridize in bonding and antibonding combinations, separated by an energy:

$$[\Delta E]_{U=0} = 2t_{\text{eff}}. \tag{5}$$

The effective Coulomb repulsion is found by computing the overlap integral for the frontier states labeled 1 and 2:

$$U_{\text{eff}} = U|\langle\psi_1|\psi_2\rangle|^2 = U\sum_i^{\text{sites}}|c_{i,1}|^2|c_{i,2}|^2. \tag{6}$$

For the 9_2-AGNR (taking $U = 3.5$), $t_{\text{eff}} = 256$ meV and $U_{\text{eff}} = 267$ meV, so that $U \sim t$, and the ribbon is on the brink of the magnetic phase transition from closed to open shell. For the 9_6-AGNR, $t_{\text{eff}} = 4$ meV and $U_{\text{eff}} = 240$ meV, so that $U_{\text{eff}} \gg t_{\text{eff}}$, and the ribbon is locked into the antiferromagnetic ground state. The same analysis reveals that the threshold for the 5_n-AGNR around $n = 10$ is associated with a decrease of the effective hybridization energy t_{eff} relative to U_{eff} for increasing n, with both $\sim$100 meV at the threshold. Note

that t_{eff} increases with an increased tail of the end state and may therefore be thought to be inversely proportional to the bandgap. Here, t_{eff} is more strongly correlated to the inverse width of the GNR, as the end states in wider GNRs localize more strongly on the zigzag edges than expected purely based on a simple bandgap argument [110]. Nevertheless, the parameters U_{eff} and t_{eff} can still be extracted empirically, and the effective Hubbard model is always valid. Also, for simplicity, we neglect the possibility of the system assuming a multireference ground state; calculations in this regard might show interesting phenomena close to a quantum phase transition, but this is beyond the scope of this paper [111].

(b) The chemical picture: Kekulé resonances and Clar sextets. More intuition can be gained using a seemingly different but ultimately analogous framework developed within the chemistry community [111–117]. The last column of Fig. 3(a) shows Kekulé resonance structures for the different N-AGNRs. The contribution of a resonance structure to the overall electronic configuration of a molecule is most significant if the total energy associated with this localized electron distribution is lowest. The energy associated with creating a pair of radicals by formally breaking the p-orbital overlap of a double bond ($\sim$70–80 kcal mol^{-1}) represents an increase in energy and usually leads to only an insignificant contribution of the associated resonance structure to the total energy. If the electronic configuration of the open-shell resonance structure, however, can give rise to an increase in the number of isolated Clar sextets, each associated with the formal resonance stabilization of a benzene ring ($\sim$36 kcal mol^{-1}), the total energy of the open-shell electron configuration can be significantly reduced, and in turn its contribution to the overall electronic configuration of a molecule increases. This explains, for example, why the 11-AGNR displays unusual behavior, and why it belongs to a different topological class than its narrower counterparts. As seen in Fig. 3(d), a resonance structure with more Clar sextets (6 Clar sextets) than both the closed-shell (2 Clar sextets) and biradical (5 Clar sextets) configurations can emerge [112,116]. Indeed, for larger values of n, the new interface states, which had overtaken the spin-split states and had a delocalized appearance in the 11_6-AGNR, eventually also start to split, thus creating a second pair of radicals. This can also be seen in Fig. 3(c), where for $n<11$, a new decay in the frontier states is observed. An even number of radicals per terminus is associated with a trivial topological phase, so that $\mathbb{Z}_2 = 0$, but the 11-AGNR with its extended zigzag edges eventually displays polyradical behavior [41,45,112].

D. 5/7-AGNR heterostructures: Electrostatics and NDR

1. Importance of electrostatics in GNR heterostructures

The transport model and the concepts of GNR topology, eigenstate localization, and impact on conductance established in the previous sections provide a powerful intellectual framework to better understand charge transport in GNR heterostructures such as 5/7-AGNRs. These heterostructures may exhibit zero modes in the form of end states and, in some cases, interface states. The emergence of the latter may be understood from the framework of 1D topology but may equivalently be rationalized by observing the local sublattice imbalance presented by the short zigzag edges of the interface (see Sec. 5 of the Supplemental Material [90]; see also Refs. [41–43,118–123] therein) [30,44,45,114–117,124–127]. What had been missing in the model so far, though, was the effect of charging. When a GNR is subjected to a voltage, three electrostatic effects come into play: (1) Application of a positive bias on the tip increases its electrostatic potential, and when the bias is sufficiently large, then vacant orbitals may become accessible for resonant transport of electrons. The opposite is true for hole transport. (2) The GNR experiences Stark shifting of its orbitals depending on their proximity to the tip or surface. (3) The orbitals and charge distribution in the GNRs will rearrange depending on the electrostatic potential landscape brought by both the tip bias and the orbitals. In general, NDR in GNRs has its origin in the Stark shifting of energy states or bands relative to resonant states, minigaps, or transport antiresonances (where the latter may occur due to quantum interference) and can therefore not be simulated in a zero-bias transmission model [8,61,62,64–67,128,129]. We therefore switch to a finite-bias transport model, based on the Hamiltonian:

$$\hat{H} = \sum_{i,\sigma}^{\text{sites}} \varepsilon_0 c_{i,\sigma}^{\dagger} c_{i,\sigma} + \sum_{\langle i,j\rangle,\sigma}^{\text{pairs}} t_{ij}(c_{i,\sigma}^{\dagger} c_{j,\sigma} + c_{i,\sigma}^{\dagger} c_{j,\sigma}) + \sum_{i}^{\text{sites}} U(n_{i\uparrow}\langle n_{i\downarrow}\rangle + \langle n_{i\uparrow}\rangle n_{i\downarrow} - \langle n_{i\uparrow}\rangle\langle n_{i\downarrow}\rangle) + \sum_{i}^{\text{sites}} eV_i. \quad (7)$$

This is an extension of our earlier model, now incorporating electrostatics. The electrostatic potential V is determined from the charge density through the Poisson equation, while the charge density is calculated within the NEGF work from the Green's function and orbital structure obtained from diagonalization of the Hamiltonian. Thus, the finite-bias transport model requires iterations of a MFH-NEGF-Poisson loop to self-consistency. The model is described in more detail in Sec. 1 of the Supplemental Material [90]. As a first test of this model, we explored the effect of the electrostatics on topologically trivial and topologically nontrivial 5/7-AGNR heterojunctions, as described in detail in Sec. 5 of the Supplemental Material [90]. The results can be summarized by stating that the bias drops predominantly over the wide-gap GNR part of the heterojunction, while the topological nature of the junction plays a relatively insignificant role.

2. Understanding NDR in 5/7-AGNR straddling gap heterostructures

(a) The 5/7/5-AGNR heterostructure: Electronic structure. The first experimental demonstration of NDR inside a single GNR came from earlier work on topologically trivial 5/7-AGNR heterostructures [65]. The structure giving the most pronounced NDR feature was the $5_4 7_8 5_4^t$-AGNR that was lifted to the point of near detachment from the surface [where the superscript t indicates that the interface is *trans* as opposed to *cis* (c) relative to the previous interface]. Using the framework established in the previous section, we now aim to analyze and understand the transport. The first step is identifying the molecular orbitals that can carry resonant transport: the building blocks of the conductance profile. Figure 4(a) shows several calculated orbitals of the $5_4 7_8 5_4^t$-AGNR close

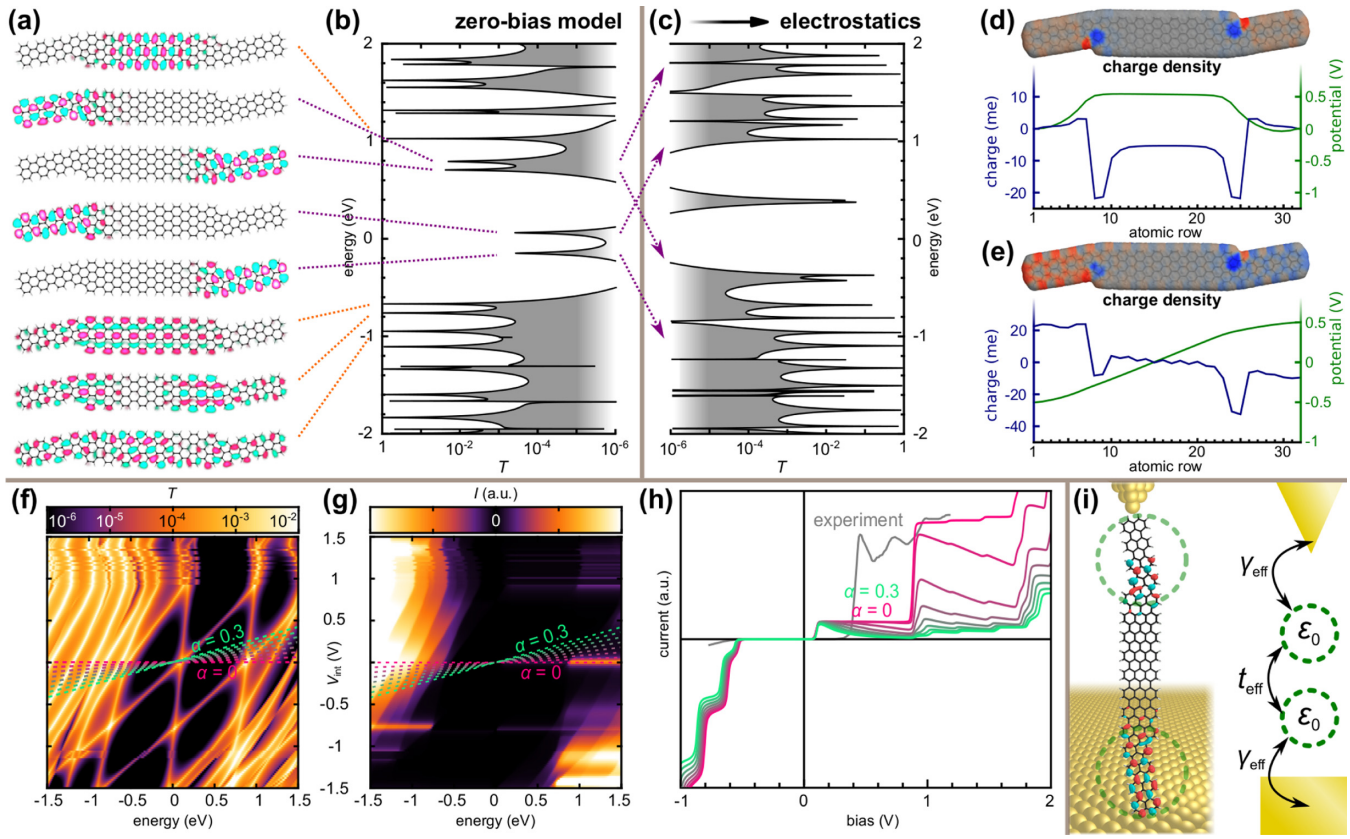

FIG. 4. Negative differential resistance (NDR) in a 5/7/5-armchair graphene nanoribbon (AGNR) tunnel junction. (a) Calculated frontier orbitals of the $5_4 7_8 5_4^t$-AGNR. (b) Calculated zero-bias transmission. (c) Calculated transmission after application of a 1 V internal bias drop. (d) Charge distribution isosurface (top), and charge per atomic row, and potential energy per atomic row in the $5_4 7_8 5_4^t$-AGNR. (e) Charge distribution isosurface (top), charge per atomic row, and potential energy per atomic row in the $5_4 7_8 5_4^t$-AGNR after application of a 1 V internal bias drop. (f) Calculated transmission as a function of energy and internal bias drop. (g) Calculated total current as a function of energy and bias drop. The diagonals represent different fractions of internal to external bias drop. (h) Calculated $I(V)$ curves for different values of α, corresponding to the cross-sections along the diagonals indicated in (g). The gray curve is the experimental result, reproduced from Jacobse *et al.* [65]. (i) The 5/7/5-AGNR tunnel junction lifted off the gold surface by the scanning tunneling microscope (STM) tip with frontier orbitals shown, schematically coarse grained into an effective two-site model.

to the Fermi level. The second step is to identify zero modes or topological character. From the previous section, the $5_4 7_8 5_4^t$-AGNR is readily identified as a topologically trivial double junction, but its 5-AGNR ends will give rise to topological end states which may delocalize enough to also have some presence in the ends of the 7-AGNR segment. The heterostructure may equivalently be understood as a regular 5-AGNR, with a 7-AGNR potential energy barrier in the middle to spatially separate its end states and ensure an open-shell ground state. In accordance with the procedure established in Sec. III C 2 a [Eqns. (5) and (6)], the open-shell nature of this ribbon is corroborated by repeating the calculation for $U = 0$, which shows that, for both pairs of states, $t_{\text{eff}} = 6\,\text{meV}$, much weaker than the effective Coulomb interaction of $U_{\text{eff}} = 50\,\text{meV}$. In addition to the end states, the straddling-gap nature of this heterostructure permits a second pair of 5-AGNR-localized states to exist within the 7-AGNR gap at positive energy. Despite their similarity to the zero modes, these are not topological in origin. Interestingly, these also assume an open-shell, spin-split character, which is not an effect of their mutual exchange (since they are vacant) but due to their exchange with respect to the topological pair of end-localized SOMOs.

Experimentally, the presence of (pairs of) 5-AGNR-localized modes at two distinct energies within the 7-AGNR gap was verified by STS measurements [65]. On Au(111), the first pair was found at $V = 0.1\,\text{V}$, while the second pair showed up at $V = 0.8\,\text{V}$. The fact that the topological pair is found at positive bias in the form of a NIR and that neither an inelastic tunneling fingerprint nor Kondo resonance is observed $\sim$0 V is a clear indication that the states are vacant on the gold, and the GNR incurs a positive charge. This is explained by the relatively high work function of the gold surface.

(b) Relating the NDR to the frontier states. NDR in this GNR was identified when the ribbon was fully suspended from the surface, almost to the point of detachment. Near detachment suggests that the GNR-surface coupling is reduced to a strength of the same order of magnitude as the GNR-tip coupling. Therefore, we model the tip-ribbon-surface junction by applying a coupling of $i(\gamma/2) = 67i$ meV to the tip and surface on the leftmost and rightmost carbon atoms of the ribbon. The zero-bias transmission, shown in Fig. 4(b), reveals that unimpeded transport—associated with a maximum transmission per spin channel of the conductance quantum—is

solely possible for the states outside the 7-AGNR transport gap of −0.8 to 0.8 V. This result agrees with the straddling gap nature of the 5/7-AGNR and the intuition built from the results from Secs. III A and III C. The pairs of 5-AGNR-localized states, given their physical separation, give rise to transport resonances two and four orders of magnitude lower than the other peaks, respectively, quite like the impeded transport through frontier states in open-shell AGNRs as established in Sec. III C. It is the tunneling between these resonant states and their Stark shifting relative to each other upon applied bias that is ultimately responsible for the emergence of NDR in the low-bias regime since experimentally the NDR is observed within the 7-AGNR transport gap [see Fig. 4(h)] [65].

(c) Effect of the applied bias. Figure 4(d) shows the charge distribution and electrostatic potential per atomic row for this GNR at charge neutrality, revealing a charge accumulation on the five-membered rings. Upon application of an internal bias voltage drop of $V_{\text{int}} = 1$ V, the 5-AGNR ends incur positive and negative charge by injection of holes and electrons into them, while the 7-AGNR segment remains neutral, which is shown in Fig. 4(e). In this calculation, the Fermi level was set to $E_{\text{F}} = 0.5$ V, so that the potential drop is symmetric, and the left side of the ribbon experiences as much negative bias as the right-side experiences positive bias. Since the end states are topological zero modes, charge is readily injected into them upon application of a bias voltage. These charged regions ensure that the electrostatic potential assumes a roughly sigmoidal profile inside the ribbon, as is evident from Fig. 4(e). The new transmission profile that emerges under the biased condition is shown in Fig. 4(c).

(d) Analyzing the transmission profile. Figure 4(f) shows the calculated transmission as a function of energy and internal bias drop V_{int} (this time relative to the voltage of the surface instead of the Fermi level of the GNR since the surface is assumed to be at ground in the calculations). Transport resonances that originate from orbitals that span across the length of the nanoribbon incur a Stark shift of ∼0.5 eV/V of internal bias drop. The resonances originating from the 5-AGNR localized states are seen at lower bias, and by contrast with the delocalized states, these shift by ∼1 eV/V for the state in contact with the tip and by 0 eV/V for the state in contact with the surface. This is true for both pairs of 5-AGNR-localized states identified before, resulting in a checkered pattern in the low-bias regime as they cross one another.

Figure 4(g) shows the total current $I(E, V)$ as a function of energy and internal bias drop V_{int}. Even though, for each constant value of the internal bias drop, the current is a monotonically increasing function with energy (horizontal cross-sections), the current can exhibit NDR when the internal bias drop increases with charge carrier energy such that the current is described by a diagonal rather than a horizontal cross-section of the diagram. In the case of this nanoribbon, transport resonances coming from the pairs of 5-AGNR localized states rapidly disappear with increasing bias voltage drop. Figure 4(h) shows several simulated $I(V)$ curves corresponding to different cross-sections of the $I(E, V)$ data, as indicated in Fig. 4(g). These cross-sections signify different amounts of internal bias drop in relation to charge carrier energy, quantified by the parameter α (Sec. 5 of the Supplemental Material [90]). Here, $\alpha = 0$ corresponds to a horizontal cross-section, where the bias drop is purely external, over the contacts, so that there is no Stark shifting and NDR is not possible: the transport reflects the zero-bias transmission. Also, $\alpha = 1$ corresponds to a 45 ° cross-section, where all bias drop is internal, and Stark shifting is maximal. A reasonable estimate for α, assuming most of the bias drop is still over the contacts, should roughly be in the range of $\alpha = 0$–0.3. Indeed, any nonzero value of α is seen to qualitatively reproduce the experimental features (large and monotonically increasing current in the high-bias regime, a peaked onset followed by a slight decay in the current in the low-bias regime).

Evidently, the 5-AGNR-localized states are initially degenerate [the intersections of the checkered pattern on the horizontal axis of Fig. 4(f)] and initially contribute to the current but are slowly pulled apart electrostatically with increasing internal bias voltage drop, resulting in quenching of their resonance and suppression of current at higher bias. This scenario is well known in the literature and can equivalently be captured in an effective tight-binding transport model which is coarse grained into just two mutually interacting sites that are subjected to the Stark effect, as shown in Fig. 4(i) [130–133]. The effective model readily reproduces the peaked, decaying onset of the experiment.

3. Anomalous NDR in a 7/5/7-AGNR

(a) Experimental observation of anomalous NDR. To further validate the transport model, we performed an *in situ* lifting experiment on another 5/7-AGNR heterostructure: the $7_2 5_2 7_8^c$-AGNR [shown schematically in Fig. 5(g)]. This GNR was synthesized by means of the standard codeposition of a mixture of 3,9-dibromoperylene/3,10-dibromoperylene and 10,10′-dibromo-9,9′-bianthryl (DBBA) on Au(111), followed by stepwise annealing [65]. Its structure can be understood as a 7_{12}-AGNR [shown schematically in Fig. 5(h)] with a 5-AGNR notch near one of its ends. Figure 5(a) shows a map of the differential conductance $dI/dV(V, z)$ as a function of tip-substrate distance z and bias voltage V applied to the $7_2 5_2 7_8^c$-AGNR while lifted from the notched end. The conductance map of this GNR on NaCl reveals resonant transport onsets at $V = -1$ and 2 V, where the differential conductance reaches values of ∼100 nS, in agreement with the regular 7-AGNR [86], an additional, persistent in-gap feature around $V = -0.5$ V, and a dramatic NDR with the differential conductance reaching values of −100 nS at bias voltages just past the HOMO onset at −1 V. The NDR is seen in more detail in the $I(V)$ spectra shown in Fig. 5(b).

(b) Electronic structure and simulated transport profile. The calculated frontier orbitals for this GNR are shown in Fig. 5(d). Figure 5(c) shows STM topographic scans of the GNR after transfer to the NaCl adlayer, in general agreement with superpositions of the calculated eigenstates. The image at $V = -0.5$ V reveals resonant tunneling through the end state that is extended through the notch and causes the nonvanishing −0.5 V resonance. The calculated transmission is shown in Fig. 5(g) for the $7_2 5_2 7_8^c$-AGNR and in Fig. 5(h) for the 7_{12}-AGNR, with the latter being included for the sake of comparison. The behavior of the end states, with those in contact with the tip shifting rigidly with the applied bias and those in contact with the surface hardly shifting at all, agrees

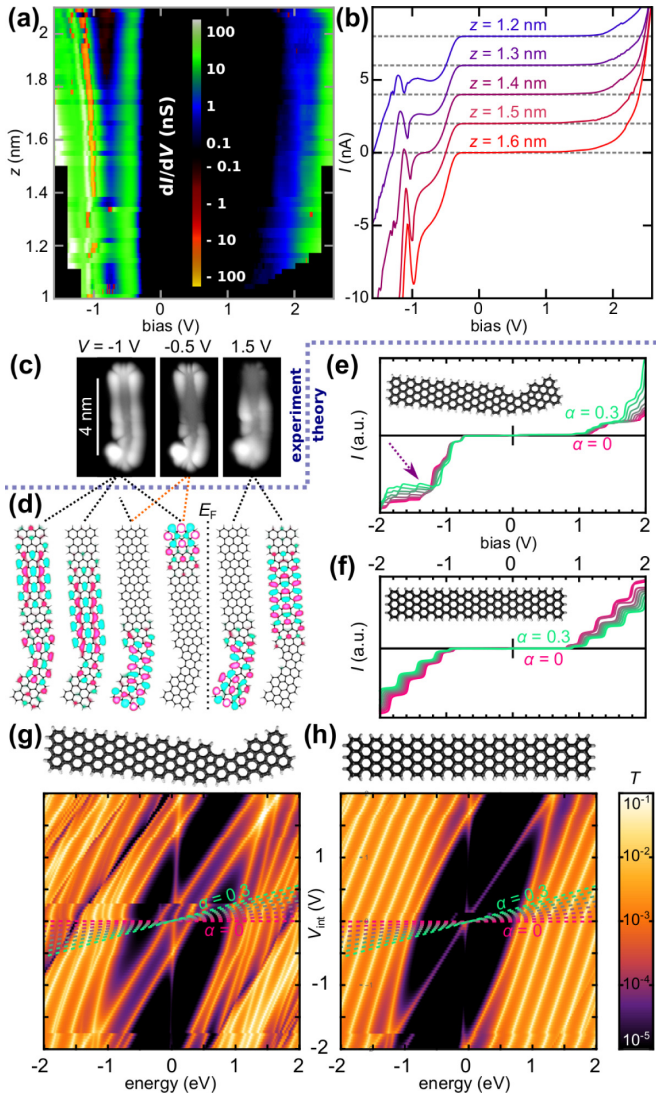

FIG. 5. Transport through a notched 7-armchair graphene nanoribbon (AGNR) on NaCl, showing pronounced negative differential resistance (NDR). (a) Transport for the $7_2 5_2 7_8^c$-AGNR on NaCl as a function of lifting height z and bias voltage V. (b) Measured $I(V)$ spectra at specific heights. The curves are offset by 2 nA for clarity. (c) Scanning tunneling microscope (STM) scans ($I = 30$ pA, bias voltage as indicated) of the $7_2 5_2 7_8^c$-AGNR on NaCl. (d) Calculated frontier orbitals of the $7_2 5_2 7_8^c$-AGNR. (e) Calculated $I(V)$ curves for the $7_2 5_2 7_8^c$-AGNR. (f) Calculated $I(V)$ curves for the 7_{12}-AGNR. (g) Calculated transmission as a function of energy and internal bias drop for the $7_2 5_2 7_8^c$-AGNR on NaCl. (h) Calculated transmission as a function of energy and internal bias drop of the 7_{12}-AGNR on NaCl.

with the results obtained on the $5_4 7_8 5_4^t$-AGNR (Sec. III D 2 d). Spin splitting occurs around charge neutrality ($V_{\text{int}} = 0$) but is quenched when the applied bias is strong enough to pull the end states apart energetically. For the 7_{12}-AGNR, outside the transport gap, electronic states experience a quite rigid shift with applied bias with no appreciable relative shifting or crossing between them. In the case of the $7_2 5_2 7_8^c$-AGNR, shown in Fig. 5(g), the low-energy region features nondegenerate end states due to the different nature of the two termini (notched vs pristine). A more complex pattern of (avoided) level crossings is seen this time as the nonsymmetric nature of the GNR induces different states to localize predominantly on either the notched side or the pristine side of the nanoribbon. Transport antiresonances—likely caused by destructive quantum interference induced by the five-membered rings [61,130]—are now also observed, where the transmission abruptly drops to zero.

(c) Nonuniform level shifting causes NDR. Figure 5(e) shows calculated $I(V)$ curves for the $7_2 5_2 7_8^c$-AGNR for α ranging from 0 to 0.3. For $\alpha = 0.3$, the experimental observations are reproduced qualitatively: the weak onset at negative bias is followed by a stronger onset with a distinct subsequent NDR feature. In accordance with experiment, this does not happen on the conduction band side, where the current increases monotonically for every value of α. For the unperturbed 7_{12}-AGNR, NDR is never observed [Fig. 5(f)]. This reveals a general phenomenon: the absence of resonant crossings, fading transport resonances, transport antiresonances, minigaps, or any sort of handle precludes the emergence of NDR [Fig. 5(h)]. It can therefore be concluded that the NDR in topological GNR heterostructures—even the very nontrivial $7_2 5_2 7_8^c$-AGNR—originates from the intricate shifting, charge redistribution, and changes in eigenstate localization—effects that are absent in pristine AGNRs by nature of the fully delocalized nature of all eigenstates. Note that, in the case of the $7_2 5_2 7_8^c$-AGNR, NDR cannot be reduced to something as straightforward as the effective two-site model as was the case for the $5_4 7_8 5_4^t$-AGNR. However, NDR still arises from a concerted interplay of the electronic structure of the nanoribbon and is effectively captured in the model.

IV. DISCUSSION AND CONCLUSIONS

We have performed transport experiments on topological GNRs and GNR heterojunctions and developed a framework to simulate through-transport experiments on GNRs and GNR heterostructures. Our model qualitatively accounts for experimental observations published in the literature as well as transport experiments presented here. Transport effects due to nanoribbon topology, length, structure, zero modes, and applied bias were discussed and a transport model developed to capture the relevant physics of transport in topological GNRs and GNR heterostructures. In doing so, we could put into perspective some important emergent effects in transport.

Specifically, we showed how through-transport obscures modes (both topological zero modes and other localized states) that are present in the GNR and observable in regular STS measurements but do not contribute to transport because of their localized character. Short topologically nontrivial GNRs feature enhanced transport through the (hybridized) end states, while the contribution of frontier states vanishes with increasing ribbon length. Both the open- and closed-shell regimes are accessible in transport, which is now experimentally verified by measurements in both the magnetic and diamagnetic regimes [37,80]. Similar effects are predicted for all topologically nontrivial GNRs, with the threshold between closed- and open-shell ground state and consequent enhanced or decaying transport dictated by the effective Hubbard parameters t_{eff} and U_{eff}.

We also analyzed charge transport in a 5/7/5-AGNR which had been shown to exhibit NDR, and to this end, we extended the model to a finite-bias self-consistent Hubbard-NEGF-Poisson model incorporating electrostatic effects. We establish a methodology where the transmission is analyzed as a function of internal bias drop, after which the transport profile is retrieved empirically by selecting a cross-sectional profile that reflects the correct fraction of internal to total bias drop. The theoretical $I(V)$ curve indeed exhibits the same qualitative features as the experiment, including NDR. Using this methodology, the NDR effect can now directly be traced back to Stark-induced level shifting of initially degenerate states localized on opposite ends and the consequent appearance of resonant transport between them followed by destruction of the resonance at higher bias voltage. Finally, we present an experiment on a 7/5/7-AGR that was also found to exhibit pronounced NDR. Our model allowed us to find $I(V)$ curves that reproduced the anomalous NDR effect in this nanoribbon, which occurs selectively at the valence band onset.

The model used in this paper is relatively crude and certainly has several limitations. However, the aim of this paper was to deepen the mechanisms underlying charge transport in GNRs, uncover the physical mechanisms underlying effects such as NDR in GNR heterostructures, and bridge between the experimentally accessible transport and calculations, and in that respect, it is successful. The exploration of the relationships between transport, eigenstate localization, nanoribbon topology, heterostructures, and bias-induced effects presented in this paper, as well as synergy between experimental and computational results, helps to expand our general understanding of charge transport through GNRs and GNR heterostructures.

ACKNOWLEDGMENTS

This paper was funded by the U.S. Department of Energy, Office of Science, Office of Basic Energy Sciences, Materials Sciences and Engineering Division under Contract No. DE-AC02-05-CH11231 (Nanomachine program: KC1203; development of GNR electronic structure formalism and simulations). Support was also provided by the Office of Naval Research under the MURI Program N00014-19-1-2596 (GNR lifting simulation) and the National Science Foundation under DMR-1839098 (image analysis). P.H.J. acknowledges fellowship support from the Dutch Research Council (NWO) through Rubicon Award No. 019.182EN.18. We acknowledge useful discussions with Daniel J. Rizzo, Juan Pablo Llinas, Joseph M. Thijssen, Zafer Mutlu, Franklin Liou, and Jeffrey Bokor.

[1] A. K. Geim and K. S. Novoselov, The rise of graphene, Nat. Mater. **6**, 183 (2007).

[2] A. H. Castro Neto, F. Guinea, N. M. R. Peres, K. S. Novoselov, and A. K. Geim, The electronic properties of graphene, Rev. Mod. Phys. **81**, 109 (2009).

[3] N. Tombros, C. Jozsa, M. Popinciuc, H. T. Jonkman, and B. J. van Wees, Electronic spin transport and spin precession in single graphene layers at room temperature, Nature (London) **448**, 571 (2007).

[4] W. Han, R. K. Kawakami, M. Gmitra, and J. Fabian, Graphene spintronics, Nat. Nanotechnol. **9**, 794 (2014).

[5] J. Baringhaus, M. Ruan, F. Edler, A. Tejeda, M. Sicot, A. Taleb-Ibrahimi, A.-P. Li, Z. Jiang, E. H. Conrad, C. Berger, C. Tegenkamp, and W. A. de Heer, Exceptional ballistic transport in epitaxial graphene nanoribbons, Nature (London) **506**, 349 (2014).

[6] H. Zheng, Z. F. Wang, T. Luo, Q. W. Shi, and J. Chen, Analytical study of electronic structure in armchair graphene nanoribbons, Phys. Rev. B **75**, 165414 (2007).

[7] Y. W. Son, M. L. Cohen, and S. G. Louie, Energy Gaps in Graphene Nanoribbons, Phys. Rev. Lett. **97**, 216803 (2006).

[8] S. Smith, J. Llinás, J. Bokor, and S. Salahuddin, Negative differential resistance and steep switching in chevron graphene nanoribbon field-effect transistors, IEEE Electron Device Lett. **39**, 143 (2018).

[9] P. B. Bennett, Z. Pedramrazi, A. Madani, Y.-C. Chen, D. G. de Oteyza, C. Chen, F. R. Fischer, M. F. Crommie, and J. Bokor, Bottom-up graphene nanoribbon field-effect transistors, Appl. Phys. Lett. **103**, 253114 (2013).

[10] E. U. Stützel, M. Burghard, K. Kern, F. Traversi, F. Nichele, and R. Sordan, A graphene nanoribbon memory cell, Small **6**, 2822 (2010).

[11] J. Cai, P. Ruffieux, R. Jaafar, M. Bieri, T. Braun, S. Blankenburg, M. Muoth, A. P. Seitsonen, M. Saleh, X. Feng, K. Müllen, and R. Fasel, Atomically precise bottom-up fabrication of graphene nanoribbons, Nature (London) **466**, 470 (2010).

[12] L. Martini, Z. Chen, N. Mishra, G. B. Barin, P. Fantuzzi, P. Ruffieux, R. Fasel, X. Feng, A. Narita, C. Coletti, K. Müllen, and A. Candini, Structure-dependent electrical properties of graphene nanoribbon devices with graphene electrodes, Carbon **146**, 36 (2019).

[13] Z. Geng, B. Hähnlein, R. Granzner, M. Auge, A. A. Lebedev, V. Y. Davydov, M. Kittler, J. Pezoldt, and F. Schwierz, Graphene nanoribbons for electronic devices, Ann. Phys. **529**, 1700033 (2017).

[14] F. Schwierz, Graphene transistors, Nat. Nanotechnol. **5**, 487 (2010).

[15] B. Hähnlein, B. Händel, J. Pezoldt, H. Töpfer, R. Granzner, and F. Schwierz, Side-gate graphene field-effect transistors with high transconductance, Appl. Phys. Lett. **101**, 093504 (2012).

[16] P. Shemella, Y. Zhang, M. Mailman, P. M. Ajayan, and S. K. Nayak, Energy gaps in zero-dimensional graphene nanoribbons, Appl. Phys. Lett. **91**, 042101 (2007).

[17] M. Y. Han, B. Özyilmaz, Y. Zhang, and P. Kim, Energy Band-Gap Engineering of Graphene Nanoribbons, Phys. Rev. Lett. **98**, 206805 (2007).

[18] M. Kariminezhad and A. Namiranian, Spin-polarized transport in zigzag graphene nanoribbons with Rashba spin-orbit interaction, J. Appl. Phys. **110**, 103702 (2011).

[19] M. Droth and G. Burkard, Electron spin relaxation in graphene nanoribbon quantum dots, Phys. Rev. B **87**, 205432 (2013).

[20] Z. F. Wang, Q. Li, Q. W. Shi, X. Wang, J. G. Hou, H. Zheng, and J. Chen, Ballistic rectification in a Z-shaped graphene nanoribbon junction, Appl. Phys. Lett. **92**, 133119 (2008).

[21] O. V. Yazyev, A guide to the design of electronic properties of graphene nanoribbons, Acc. Chem. Res. **46**, 2319 (2013).

[22] O. V. Yazyev, Emergence of magnetism in graphene materials and nanostructures, Rep. Prog. Phys. **73**, 056501 (2010).

[23] K. Nakada, M. Fujita, G. Dresselhaus, and M. S. Dresselhaus, Edge state in graphene ribbons: Nanometer size effect and edge shape dependence, Phys. Rev. B **54**, 17954 (1996).

[24] M. Ezawa, Peculiar width dependence of the electronic properties of carbon nanoribbons, Phys. Rev. B **73**, 045432 (2006).

[25] D. E. Jiang, B. G. Sumpter, and S. Dai, Unique chemical reactivity of a graphene nanoribbon's zigzag edge, J. Chem. Phys. **127**, 124703 (2007).

[26] M. Fujita, K. Wakabayashi, K. Nakada, and K. Kusakabe, Peculiar localized state at zigzag graphite edge, J. Phys. Soc. Jpn. **65**, 1920 (1996).

[27] P. Ruffieux, S. Wang, B. Yang, C. Sanchez-Sanchez, J. Liu, T. Dienel, L. Talirz, P. Shinde, C. A. Pignedoli, D. Passerone, T. Dumslaff, X. Feng, K. Müllen, and R. Fasel, On-surface synthesis of graphene nanoribbons with zigzag edge topology, Nature (London) **531**, 489 (2016).

[28] P. P. Shinde, O. Gröning, S. Wang, P. Ruffieux, C. A. Pignedoli, R. Fasel, and D. Passerone, Stability of edge magnetism in functionalized zigzag graphene nanoribbons, Carbon **124**, 123 (2017).

[29] Z. F. Wang, Q. Li, H. Zheng, H. Ren, H. Su, Q. W. Shi, and J. Chen, Tuning the electronic structure of graphene nanoribbons through chemical edge modification: A theoretical study, Phys. Rev. B **75**, 113406 (2007).

[30] J. Li, S. Sanz, M. Corso, D. J. Choi, D. Peña, T. Frederiksen, and J. I. Pascual, Single spin localization and manipulation in graphene open-shell nanostructures, Nat. Commun. **10**, 200 (2019).

[31] S. Mishra, D. Beyer, K. Eimre, S. Kezilebieke, R. Berger, O. Gröning, C. A. Pignedoli, K. Müllen, P. Liljeroth, P. Ruffieux, X. Feng, and R. Fasel, Topological frustration induces unconventional magnetism in a nanographene, Nat. Nanotechnol. **15**, 22 (2020).

[32] S. Mishra, X. Yao, Q. Chen, K. Eimre, O. Gröning, R. Ortiz, M. D. Giovannantonio, J. Sancho-García, J. Fernández-Rossier, C. A. Pignedoli, K. Müllen, P. Ruffieux, A. Narita, and R. Fasel, Large magnetic exchange coupling in rhombus-shaped nanographenes with zigzag periphery, Nat. Chem. **13**, 581 (2021).

[33] S. Mishra, D. Beyer, K. Eimre, R. Ortiz, J. Fernández-Rossier, R. Berger, O. Gröning, C. A. Pignedoli, R. Fasel, X. Feng, and P. Ruffieux, Collective all-carbon magnetism in triangulene dimers, Angew. Chemie Int. Ed. **59**, 12041 (2020).

[34] J. Li, S. Sanz, J. Castro-Esteban, M. Vilas-Varela, N. Friedrich, T. Frederiksen, D. Peña, and J. I. Pascual, Uncovering the Triplet Ground State of Triangular Graphene Nanoflakes Engineered with Atomic Precision on a Metal Surface, Phys. Rev. Lett. **124**, 177201 (2020).

[35] S. Mishra, D. Beyer, R. Berger, J. Liu, O. Gröning, J. I. Urgel, K. Müllen, P. Ruffieux, X. Feng, and R. Fasel, Topological defect-induced magnetism in a nanographene, J. Am. Chem. Soc. **142**, 1147 (2020).

[36] S. Song, J. Su, M. Telychko, J. Li, G. Li, Y. Li, C. Su, J. Wu, and J. Lu, On-surface synthesis of graphene nanostructures with π-magnetism, Chem. Soc. Rev. **50**, 3238 (2021).

[37] J. Lawrence, P. Brandimarte, A. Berdonces-Layunta, M. S. G. Mohammed, A. Grewal, C. C. Leon, D. Sánchez-Portal, and D. G. De Oteyza, Probing the magnetism of topological end states in 5-armchair graphene nanoribbons, ACS Nano **14**, 4499 (2020).

[38] A. Sánchez-Grande, J. I. Urgel, A. Cahlík, J. Santos, S. Edalatmanesh, E. Rodríguez-Sánchez, K. Lauwaet, P. Mutombo, D. Nachtigallová, R. Nieman, H. Lischka, B. de la Torre, R. Miranda, O. Gröning, N. Martín, P. Jelínek, and D. Écija, Diradical organic one-dimensional polymers synthesized on a metallic surface, Angew. Chemie Int. Ed. **59**, 17594 (2020).

[39] Y. Zheng, C. Li, C. Xu, D. Beyer, X. Yue, Y. Zhao, G. Wang, D. Guan, Y. Li, H. Zheng, C. Liu, J. Liu, X. Wang, W. Luo, X. Feng, S. Wang, and J. Jia, Designer spin order in diradical nanographenes, Nat. Commun. **11**, 6076 (2020).

[40] Y. Zheng, C. Li, Y. Zhao, D. Beyer, G. Wang, C. Xu, X. Yue, Y. Chen, D.-D. Guan, Y.-Y. Li, H. Zheng, C. Liu, W. Luo, X. Feng, S. Wang, and J. Jia, Engineering of Magnetic Coupling in Nanographene, Phys. Rev. Lett. **124**, 147206 (2020).

[41] T. Cao, F. Zhao, and S. G. Louie, Topological Phases in Graphene Nanoribbons: Junction States, Spin Centers, and Quantum Spin Chains, Phys. Rev. Lett. **119**, 076401 (2017).

[42] O. Gröning, S. Wang, X. Yao, C. A. Pignedoli, G. Borin Barin, C. Daniels, A. Cupo, V. Meunier, X. Feng, A. Narita, K. Müllen, P. Ruffieux, and R. Fasel, Engineering of robust topological quantum phases in graphene nanoribbons, Nature (London) **560**, 209 (2018).

[43] D. J. Rizzo, G. Veber, T. Cao, C. Bronner, T. Chen, F. Zhao, H. Rodriguez, S. G. Louie, M. F. Crommie, and F. R. Fischer, Topological band engineering of graphene nanoribbons, Nature (London) **560**, 204 (2018).

[44] Y.-L. Lee, F. Zhao, T. Cao, J. Ihm, and S. G. Louie, Topological phases in cove-edged and chevron graphene nanoribbons: Geometric structures, $\mathbb{Z}_2$ invariants, and junction states, Nano Lett. **18**, 7247 (2018).

[45] J. Jiang and S. G. Louie, Topology classification using chiral symmetry and spin correlations in graphene nanoribbons, Nano Lett. **21**, 197 (2021).

[46] D. J. Rizzo, G. Veber, J. Jiang, R. McCurdy, T. Cao, C. Bronner, T. Chen, S. G. Louie, F. R. Fischer, and M. F. Crommie, Inducing metallicity in graphene nanoribbons via zero-mode superlattices, Science **369**, 1597 (2020).

[47] Y. Tan, X.-S. Xia, X.-L. Liao, J.-B. Li, H.-H. Zhong, S. Liang, S. Xiao, L.-H. Liu, J.-H. Luo, M.-D. He, and L.-Q. Chen, A highly-flexible bistable switch based on a suspended monolayer Z-shaped graphene nanoribbon nanoresonator, Carbon **157**, 724 (2020).

[48] M. Pizzochero, K. Čerņevičs, G. Borin Barin, S. Wang, P. Ruffieux, R. Fasel, and O. V. Yazyev, Quantum electronic transport across "bite" defects in graphene nanoribbons, 2D Mater. **8**, 035025 (2021).

[49] L. Rosales, M. Pacheco, Z. Barticevic, A. Latgé, and P. A. Orellana, Transport properties of graphene nanoribbons with side-attached organic molecules, Nanotechnology **19**, 065402 (2008).

[50] L. Rosales, M. Pacheco, Z. Barticevic, A. Latgé, and P. A. Orellana, Conductance gaps in graphene ribbons designed by molecular aggregations, Nanotechnology **20**, 095705 (2009).

[51] K. Čerņevičs, M. Pizzochero, and O. V. Yazyev, Even-odd conductance effect in graphene nanoribbons induced by edge functionalization with aromatic molecules: Basis for novel chemosensors, Eur. Phys. J. Plus **135**, 681 (2020).

[52] M. Mehdi Pour, A. Lashkov, A. Radocea, X. Liu, T. Sun, A. Lipatov, R. A. Korlacki, M. Shekhirev, N. R. Aluru, J. W. Lyding, V. Sysoev, and A. Sinitskii, Laterally extended atomically precise graphene nanoribbons with improved electrical conductivity for efficient gas sensing, Nat. Commun. **8**, 820 (2017).

[53] S. L. Chang, B. R. Wu, P. H. Yang, and M. F. Lin, Curvature effects on electronic properties of armchair graphene nanoribbons without passivation, Phys. Chem. Chem. Phys. **14**, 16409 (2012).

[54] J. Zhang and E. P. Fahrenthold, Conductance of curved $3M-1$ armchair graphene nanoribbons, J. Phys. Chem. C **123**, 21805 (2019).

[55] C. Moreno, M. Vilas-Varela, B. Kretz, A. Garcia-Lekue, M. V. Costache, M. Paradinas, M. Panighel, G. Ceballos, S. O. Valenzuela, D. Peña, and A. Mugarza, Bottom-up synthesis of multifunctional nanoporous graphene, Science **360**, 199 (2018).

[56] G. Calogero, I. Alcón, N. Papior, A.-P. Jauho, and M. Brandbyge, Quantum interference engineering of nanoporous graphene for carbon nanocircuitry, J. Am. Chem. Soc. **141**, 13081 (2019).

[57] A. Sinitskii, A recipe for nanoporous graphene, Science **360**, 154 (2018).

[58] P. H. Jacobse, R. D. McCurdy, J. Jiang, D. J. Rizzo, G. Veber, P. Butler, R. Zuzak, S. G. Louie, F. R. Fischer, and M. F. Crommie, Bottom-up assembly of nanoporous graphene with emergent electronic states, J. Am. Chem. Soc. **142**, 13507 (2020).

[59] D. H. Zhang, K. L. Yao, and G. Y. Gao, The peculiar transport properties in *p-n* junctions of doped graphene nanoribbons, J. Appl. Phys. **110**, 013718 (2011).

[60] H. Mohamadpour and A. Asgari, Graphene nanoribbon tunneling field effect transistors, Physica E Low Dimens. Syst. Nanostruct. **43**, 1708 (2011).

[61] D. Nozaki, A. Santana-Bonilla Lokamani, A. Dianat, R. Gutierrez, and G. Cuniberti, Switchable negative differential resistance induced by quantum interference effects in porphyrin-based molecular junctions, J. Phys. Chem. Lett. **6**, 3950 (2015).

[62] Y. An, K. Wang, Z. Yang, Z. Liu, G. Jia, Z. Jiao, T. Wang, and G. Xu, Negative differential resistance and rectification effects in step-like graphene nanoribbons, Org. Electron. **17**, 262 (2015).

[63] X. Kong, B. Cui, W. Zhao, J. Zhao, D. Li, and D. Liu, Spin negative differential resistance and high spin filtering behavior realized by devices based on graphene nanoribbons and graphitic carbon nitrides, Org. Electron. **15**, 3674 (2014).

[64] Y. Zhou, N. Qiu, R. Li, Z. Guo, J. Zhang, J. Fang, A. Huang, J. He, X. Zha, K. Luo, J. Yin, Q. Li, X. Bai, Q. Huang, and S. Du, Negative differential resistance and rectifying performance induced by doped graphene nanoribbons *p-n* device, Phys. Lett. A **380**, 1049 (2016).

[65] P. H. Jacobse, A. Kimouche, T. Gebraad, M. M. Ervasti, J. M. Thijssen, P. Liljeroth, and I. Swart, Electronic components embedded in a single graphene nanoribbon, Nat. Commun. **8**, 119 (2017).

[66] G. J. Ferreira, M. N. Leuenberger, D. Loss, and J. C. Egues, Low-bias negative differential resistance in graphene nanoribbon superlattices, Phys. Rev. B **84**, 125453 (2011).

[67] P. Tseng, C. H. Chen, S. A. Hsu, and W. J. Hsueh, Large negative differential resistance in graphene nanoribbon superlattices, Phys. Lett. A **382**, 1427 (2018).

[68] Y. Ye, L. Gan, L. Dai, H. Meng, F. Wei, Y. Dai, Z. Shi, B. Yu, X. Guo, and G. Qin, Multicolor graphene nanoribbon/semiconductor nanowire heterojunction light-emitting diodes, J. Mater. Chem. **21**, 11760 (2011).

[69] M. C. Chong, N. Afshar-Imani, F. Scheurer, C. Cardoso, A. Ferretti, D. Prezzi, and G. Schull, Bright electroluminescence from single graphene nanoribbon junctions, Nano Lett. **18**, 175 (2018).

[70] C. Ma, Z. Xiao, A. A. Puretzky, H. Wang, A. Mohsin, J. Huang, L. Liang, Y. Luo, B. J. Lawrie, G. Gu, W. Lu, K. Hong, J. Bernholc, and A.-P. Li, Engineering edge states of graphene nanoribbons for narrow-band photoluminescence, ACS Nano **14**, 5090 (2020).

[71] I. Ivanov, Y. Hu, S. Osella, U. Beser, H. I. Wang, D. Beljonne, A. Narita, K. Müllen, D. Turchinovich, and M. Bonn, Role of edge engineering in photoconductivity of graphene nanoribbons, J. Am. Chem. Soc. **139**, 7982 (2017).

[72] L. Talirz, P. Ruffieux, and R. Fasel, On-surface synthesis of atomically precise graphene nanoribbons, Adv. Mater. **28**, 6222 (2016).

[73] R. S. Koen Houtsma, J. de la Rie, and M. Stöhr, Atomically precise graphene nanoribbons: Interplay of structural and electronic properties, Chem. Soc. Rev. **50**, 6541 (2021).

[74] F. Chen and N. J. Tao, Electron transport in single molecules: From benzene to graphene, Acc. Chem. Res. **42**, 429 (2009).

[75] Y. C. Chen, T. Cao, C. Chen, Z. Pedramrazi, D. Haberer, D. G. De Oteyza, F. R. Fischer, S. G. Louie, and M. F. Crommie, Molecular bandgap engineering of bottom-up synthesized graphene nanoribbon heterojunctions, Nat. Nanotechnol. **10**, 156 (2015).

[76] Q. Sun, O. Gröning, J. Overbeck, O. Braun, M. L. Perrin, G. Borin Barin, M. El Abbassi, K. Eimre, E. Ditler, C. Daniels, V. Meunier, C. A. Pignedoli, M. Calame, R. Fasel, and P. Ruffieux, Massive Dirac fermion behavior in a low bandgap graphene nanoribbon near a topological phase boundary, Adv. Mater. **32**, 1906054 (2020).

[77] J. P. Llinas, A. Fairbrother, G. Borin Barin, W. Shi, K. Lee, S. Wu, B. Y. Choi, R. Braganza, J. Lear, N. Kau, W. Choi, C. Chen, Z. Pedramrazi, T. Dumslaff, A. Narita, X. Feng, K. Müllen, F. Fischer, A. Zettl, P. Ruffieux *et al.*, Short-channel field-effect transistors with 9-atom and 13-atom wide graphene nanoribbons, Nat. Commun. **8**, 633 (2017).

[78] N. Richter, Z. Chen, A. Tries, T. Prechtl, A. Narita, K. Müllen, K. Asadi, M. Bonn, and M. Kläui, Charge transport mechanism in networks of armchair graphene nanoribbons, Sci. Rep. **10**, 1988 (2020).

[79] H. Sakaguchi, S. Song, T. Kojima, and T. Nakae, Homochiral polymerization-driven selective growth of graphene nanoribbons, Nat. Chem. **9**, 57 (2017).

[80] M. El Abbassi, M. L. Perrin, G. B. Barin, S. Sangtarash, J. Overbeck, O. Braun, C. J. Lambert, Q. Sun, T. Prechtl, A. Narita, K. Müllen, P. Ruffieux, H. Sadeghi, R. Fasel, and M. Calame, Controlled quantum dot formation in atomically engineered graphene nanoribbon field-effect transistors, ACS Nano **14**, 5754 (2020).

[81] A. Candini, L. Martini, Z. Chen, N. Mishra, D. Convertino, C. Coletti, A. Narita, X. Feng, K. Müllen, and M. Affronte, High photoresponsivity in graphene nanoribbon field-effect transistor devices contacted with graphene electrodes, J. Phys. Chem. C **121**, 10620 (2017).

[82] S. A. Jensen, R. Ulbricht, A. Narita, X. Feng, K. Müllen, T. Hertel, D. Turchinovich, and M. Bonn, Ultrafast photoconductivity of graphene nanoribbons and carbon nanotubes, Nano Lett. **13**, 5925 (2013).

[83] D. Jänsch, I. Ivanov, Y. Zagranyarski, I. Duznovic, M. Baumgarten, D. Turchinovich, C. Li, M. Bonn, and K. Müllen, Ultra-narrow low-bandgap graphene nanoribbons from bromoperylenes—synthesis and terahertz-spectroscopy, Chem. A Eur. J. **23**, 4870 (2017).

[84] M. Koch, F. Ample, C. Joachim, and L. Grill, Voltage-dependent conductance of a single graphene nanoribbon, Nat. Nanotechnol. **7**, 713 (2012).

[85] M. Koch, Z. Li, C. Nacci, T. Kumagai, I. Franco, and L. Grill, How Structural Defects Affect the Mechanical and Electrical Properties of Single Molecular Wires, Phys. Rev. Lett. **121**, 047701 (2018).

[86] P. H. Jacobse, M. J. J. Mangnus, S. J. M. Zevenhuizen, and I. Swart, Mapping the conductance of electronically decoupled graphene nanoribbons, ACS Nano **12**, 7048 (2018).

[87] L. Lafferentz, F. Ample, H. Yu, S. Hecht, C. Joachim, and L. Grill, Conductance of a single conjugated polymer as a continuous function of its length, Science **323**, 1193 (2009).

[88] P. H. Jacobse, MATHEMATB: A MATHEMATICA package for tight-binding calculations, Comput. Phys. Commun. **244**, 392 (2019).

[89] S. Wang, N. Kharche, E. Costa Girão, X. Feng, K. Müllen, V. Meunier, R. Fasel, and P. Ruffieux, Quantum dots in graphene nanoribbons, Nano Lett. **17**, 4277 (2017).

[90] See Supplemental Material at http://link.aps.org/supplemental/10.1103/PhysRevB.105.115424 for methods, mathematical derivations, and further discussions.

[91] C. Ma, L. Liang, Z. Xiao, A. A. Puretzky, K. Hong, W. Lu, V. Meunier, J. Bernholc, and A.-P. Li, Seamless staircase electrical contact to semiconducting graphene nanoribbons, Nano Lett. **17**, 6241 (2017).

[92] A. Kimouche, M. M. Ervasti, R. Drost, S. Halonen, A. Harju, P. M. Joensuu, J. Sainio, and P. Liljeroth, Ultra-narrow metallic armchair graphene nanoribbons, Nat. Commun. **6**, 10177 (2015).

[93] Y. Hancock, A. Uppstu, K. Saloriutta, A. Harju, and M. J. Puska, Generalized tight-binding transport model for graphene nanoribbon-based systems, Phys. Rev. B **81**, 245402 (2010).

[94] A. D. Zdetsis, Bridging the physics and chemistry of graphene(s): From Hückel's aromaticity to Dirac's cones and topological insulators, J. Phys. Chem. A **124**, 976 (2020).

[95] C. J. O. Verzijl, J. S. Seldenthuis, and J. M. Thijssen, Applicability of the wide-band limit in DFT-based molecular transport calculations, J. Chem. Phys. **138**, 094102 (2013).

[96] X. Su, Z. Xue, G. Li, and P. Yu, Edge state engineering of graphene nanoribbons, Nano Lett. **18**, 5744 (2018).

[97] W. Jaskólski, A. Ayuela, M. Pelc, H. Santos, and L. Chico, Edge states and flat bands in graphene nanoribbons with arbitrary geometries, Phys. Rev. B **83**, 235424 (2011).

[98] K. Wakabayashi, K. Sasaki, T. Nakanishi, and T. Enoki, Electronic states of graphene nanoribbons and analytical solutions, Sci. Technol. Adv. Mater. **11**, 054504 (2010).

[99] L. Talirz, H. Söde, J. Cai, P. Ruffieux, S. Blankenburg, R. Jafaar, R. Berger, X. Feng, K. Müllen, D. Passerone, R. Fasel, and C. A. Pignedoli, Termini of bottom-up fabricated graphene nanoribbons, J. Am. Chem. Soc. **135**, 2060 (2013).

[100] S. Wang, L. Talirz, C. A. Pignedoli, X. Feng, K. Müllen, R. Fasel, and P. Ruffieux, Giant edge state splitting at atomically precise graphene zigzag edges, Nat. Commun. **7**, 11507 (2016).

[101] J. Tersoff and D. R. Hamann, Theory of the scanning tunneling microscope, Phys. Rev. B **31**, 805 (1985).

[102] S. Datta, Nanoscale device modeling: The Green's function method, Superlattices Microstruct. **28**, 253 (2000).

[103] J. Li, N. Friedrich, N. Merino, D. G. de Oteyza, D. Peña, D. Jacob, and J. I. Pascual, Electrically addressing the spin of a magnetic porphyrin through covalently connected graphene electrodes, Nano Lett. **19**, 3288 (2019).

[104] J. Li, W.-D. Schneider, R. Berndt, and B. Delley, Kondo Scattering Observed at a Single Magnetic Impurity, Phys. Rev. Lett. **80**, 2893 (1998).

[105] T. W. Odom, J.-L. Huang, C. L. Cheung, and C. M. Lieber, Magnetic clusters on single-walled carbon nanotubes: The Kondo effect in a one-dimensional host, Science **290**, 1549 (2000).

[106] N. Friedrich, P. Brandimarte, J. Li, S. Saito, S. Yamaguchi, I. Pozo, D. Peña, T. Frederiksen, A. Garcia-Lekue, D. Sánchez-Portal, and J. I. Pascual, Magnetism of Topological Boundary States Induced by Boron Substitution in Graphene Nanoribbons, Phys. Rev. Lett. **125**, 146801 (2020).

[107] P. W. Anderson, Localized magnetic states in metals, Phys. Rev. **124**, 41 (1961).

[108] O. Újsághy, J. Kroha, L. Szunyogh, and A. Zawadowski, Theory of the Fano Resonance in the STM Tunneling Density of States Due to a Single Kondo Impurity, Phys. Rev. Lett. **85**, 2557 (2000).

[109] G. Guo, Z. Lin, X. Li, and T. Tu, Quantum computation with graphene nanoribbon, New J. Phys. **11**, 123005 (2009).

[110] D. J. Rizzo, J. Jiang, D. Joshi, G. Veber, C. Bronner, R. A. Durr, P. H. Jacobse, T. Cao, A. Kalayjian, H. Rodriguez, P. Butler, T. Chen, S. G. Louie, F. R. Fischer, and M. F. Crommie, Rationally designed topological quantum dots in bottom-up graphene nanoribbons, ACS Nano **15**, 20633 (2021).

[111] S. Horn, F. Plasser, T. Müller, F. Libisch, J. Burgdörfer, and H. Lischka, A comparison of singlet and triplet states for one- and two-dimensional graphene nanoribbons using multireference theory, Theor. Chem. Acc. **133**, 1511 (2014).

[112] F. Plasser, H. Pašalić, M. H. Gerzabek, F. Libisch, R. Reiter, J. Burgdörfer, T. Müller, R. Shepard, and H. Lischka, The multiradical character of one- and two-dimensional graphene nanoribbons, Angew. Chemie Int. Ed. **52**, 2581 (2013).

[113] A. Konishi, Y. Hirao, M. Nakano, A. Shimizu, E. Botek, B. Champagne, D. Shiomi, K. Sato, T. Takui, K. Matsumoto, H. Kurata, and T. Kubo, Synthesis and characterization of

teranthene: A singlet biradical polycyclic aromatic hydrocarbon having Kekulé structures, J. Am. Chem. Soc. **132**, 11021 (2010).

[114] A. Konishi, Y. Hirao, K. Matsumoto, H. Kurata, R. Kishi, Y. Shigeta, M. Nakano, K. Tokunaga, K. Kamada, and T. Kubo, Synthesis and characterization of quarteranthene: Elucidating the characteristics of the edge state of graphene nanoribbons at the molecular level, J. Am. Chem. Soc. **135**, 1430 (2013).

[115] J. Liu and X. Feng, Synthetic tailoring of graphene nanostructures with zigzag-edged topologies: Progress and perspectives, Angew. Chemie Int. Ed. **59**, 23386 (2020).

[116] Z. Sun and J. Wu, Open-shell polycyclic aromatic hydrocarbons, J. Mater. Chem. **22**, 4151 (2012).

[117] A. Konishi and T. Kubo, Benzenoid quinodimethanes, Top. Curr. Chem. **375**, 83 (2017).

[118] W. S. Hwang, P. Zhao, S. G. Kim, R. Yan, G. Klimeck, A. Seabaugh, S. K. Fullerton-Shirey, H. G. Xing, and D. Jena, Room-temperature graphene-nanoribbon tunneling field-effect transistors, NPJ 2D Mat. and Appl. **3**, 43 (2019).

[119] W. Zhang, C. Basaran, and T. Ragab, Impact of geometry on transport properties of armchair graphene nanoribbon heterojunction, Carbon **124**, 422 (2017).

[120] N. Papior, N. Lorente, T. Frederiksen, A. García, and M. Brandbyge, Improvements on non-equilibrium and transport Green function techniques: The next-generation transiesta, Comput. Phys. Commun. **212**, 8 (2017).

[121] J. Taylor, H. Guo, and J. Wang, *Ab initio* modeling of quantum transport properties of molecular electronic devices, Phys. Rev. B **63**, 245407 (2001).

[122] M. Brandbyge, J. L. Mozos, P. Ordejón, J. Taylor, and K. Stokbro, Density-functional method for nonequilibrium electron transport, Phys. Rev. B **65**, 165401 (2002).

[123] T. Ozaki, K. Nishio, and H. Kino, Efficient implementation of the nonequilibrium Green function method for electronic transport calculations, Phys. Rev. B **81**, 035116 (2010).

[124] K. Wakabayashi, S. Okada, R. Tomita, S. Fujimoto, and Y. Natsume, Edge states and flat bands of graphene nanoribbons with edge modification, J.Phys. Soc. Jpn. **79**, 034706 (2010).

[125] S. Zamani and R. Farghadan, Graphene Nanoribbon Spin-Photodetector, Phys. Rev. Applied **10**, 034059 (2018).

[126] Q. Sun, X. Yao, O. Gröning, K. Eimre, C. A. Pignedoli, K. Müllen, A. Narita, R. Fasel, and P. Ruffieux, Coupled spin states in armchair graphene nanoribbons with asymmetric zigzag edge extensions, Nano Lett. **20**, 6429 (2020).

[127] M. Pizzochero and E. Kaxiras, Imprinting tunable π-magnetism in graphene nanoribbons via edge extensions, J. Phys. Chem. Lett. **12**, 1214 (2021).

[128] D. A. Areshkin and B. K. Nikolić, Electron density and transport in top-gated graphene nanoribbon devices: First-principles Green function algorithms for systems containing a large number of atoms, Phys. Rev. B **81**, 155450 (2010).

[129] D. I. Odili, Y. Wu, P. A. Childs, and D. C. Herbert, Modeling charge transport in graphene nanoribbons and carbon nanotubes using a Schrödinger-Poisson solver, J. Appl. Phys. **106**, 024509 (2009).

[130] C. J. Lambert, Basic concepts of quantum interference and electron transport in single-molecule electronics, Chem. Soc. Rev. **44**, 875 (2015).

[131] M. L. Perrin, R. Frisenda, M. Koole, J. S. Seldenthuis, J. A. C. Gil, H. Valkenier, J. C. Hummelen, N. Renaud, F. C. Grozema, J. M. Thijssen, D. Dulić, and H. S. J. van der Zant, Large negative differential conductance in single-molecule break junctions, Nat. Nanotechnol. **9**, 830 (2014).

[132] A. Aviram and M. A. Ratner, Molecular rectifiers, Chem. Phys. Lett. **29**, 277 (1974).

[133] R. Liu, S. H. Ke, H. U. Baranger, and W. Yang, Negative differential resistance and hysteresis through an organometallic molecule from molecular-level crossing, J. Am. Chem. Soc. **128**, 6274 (2006).